



# The Young Stars in the Galactic Center

Sebastiano D. von Fellenberg<sup>1,2</sup> , Stefan Gillessen<sup>2</sup> , Julia Stadler<sup>3</sup>, Michi Bauböck<sup>4</sup>, Reinhard Genzel<sup>2,5</sup> , Tim de Zeeuw<sup>2,6</sup> ,  
Oliver Pfuhl<sup>7</sup>, Pau Amaro Seoane<sup>2,8,9,10</sup>, Antonia Drescher<sup>2</sup> , Frank Eisenhauer<sup>2</sup>, Maryam Habibi<sup>2</sup> , Thomas Ott<sup>2</sup> ,  
Felix Widmann<sup>2</sup> , and Alice Young<sup>2</sup>

<sup>1</sup> Max-Planck-Institute for Radio Astronomy, auf dem Hügel 69, D-53121 Bonn, Germany; [sfellenberg@mpifr-bonn.mpg.de](mailto:sfellenberg@mpifr-bonn.mpg.de)

<sup>2</sup> Max-Planck-Institute for Extraterrestrial Physics, Gießenbachstr. 1, D-85748 Garching, Germany

<sup>3</sup> Max-Planck-Institute for Astrophysics, Karl-Schwarzschild-Strae 1, D-85748 Garching, Germany

<sup>4</sup> University of Illinois Urbana-Champaign, 1002 W. Green Street, Urbana, IL 61801, USA

<sup>5</sup> Departments of Physics and Astronomy, Le Conte Hall, University of California, Berkeley, CA 94720, USA

<sup>6</sup> Sterrewacht Leiden, Leiden University, Postbus 9513, 2300 RA Leiden, The Netherlands

<sup>7</sup> European Southern Observatory, Karl-Schwarzschild-Strae 2, D-85748 Garching, Germany

<sup>8</sup> Institute for Multidisciplinary Mathematics, UPV, Spain

<sup>9</sup> Kavli Institute for Astronomy and Astrophysics, Peking University, People's Republic of China

<sup>10</sup> AMSS, CAS, Beijing, People's Republic of China

Received 2022 March 2; revised 2022 April 20; accepted 2022 April 21; published 2022 June 9

## Abstract

We present a large  $\sim 30'' \times 30''$  spectroscopic survey of the Galactic Center using the SINFONI IFU at the VLT. Combining observations of the last two decades we compile spectra of over 2800 stars. Using the Bracket- $\gamma$  absorption lines, we identify 195 young stars, extending the list of known young stars by 79. In order to explore the angular momentum distribution of the young stars, we introduce an isotropic cluster prior. This prior reproduces an isotropic cluster in a mathematically exact way, which we test through numerical simulations. We calculate the posterior angular momentum space as a function of projected separation from Sgr A\*. We find that the observed young star distribution is substantially different from an isotropic cluster. We identify the previously reported feature of the clockwise disk and find that its angular momentum changes as a function of separation from the black hole and thus confirm a warp of the clockwise disk ( $p \sim 99.2\%$ ). At large separations, we discover three prominent overdensities of the angular momentum. One overdensity has been reported previously, the counterclockwise disk. The other two are new. Determining the likely members of these structures, we find that as many as 75% of stars can be associated with one of these features. Stars belonging to the warped clockwise disk show a top-heavy  $K$ -band luminosity function, while stars belonging to the larger separation features do not. Our observations are in good agreement with the predictions of simulations of in situ star formation and argue for the common formation of these structures.

*Unified Astronomy Thesaurus concepts:* [Galactic center \(565\)](#)

## 1. Introduction

The first infrared observations of the Galactic Center (GC) revealed that the central region of the Milky Way is surprisingly bright (Becklin & Neugebauer 1968, 1975). Due to the advent of ever higher-resolution observations we now know that this light originates from a cluster of young, massive stars, many of them O-type or Wolf-Rayet stars, residing in the central parsec (Krabbe et al. 1991; Genzel et al. 1994; Blum et al. 1996; Simons & Becklin 1996). The presence of young stars close to the massive black hole is puzzling because star formation should be suppressed in the tidal field of the large mass. At the same time, the lifetimes of such stars are so short that they cannot have migrated from afar.

The most important clue to solving this puzzle came from resolved stellar kinematics (Genzel et al. 2000; Ghez et al. 2000; Genzel et al. 2003; Levin & Beloborodov 2003; Beloborodov et al. 2006; Lu et al. 2006; Paumard et al. 2006; Bartko et al. 2009; Lu et al. 2009). The young stars to a large extent reside in two counterrotating disks. This is now

understood as a result of their formation from massive ( $\sim 10^5 M_\odot$ ) gaseous disks a few Myr ago (Bonnell & Rice 2008; Hobbs & Nayakshin 2009). This picture is supported by the fact that the observed (and hence also initial) mass function is very top heavy (Bartko et al. 2010) and by the radial surface density profile  $\sim r^{-2}$ . Further, the dynamical structure shows a warp for the clockwise disk (Bartko et al. 2009), which might be a natural consequence of resonant relaxation (Kocsis & Tremaine 2011).

While the basic findings are agreed upon, there are several details that are not fully settled: Do et al. (2013), Lu et al. (2013), and Støstad et al. (2015) find a less top-heavy mass function than Bartko et al. (2010). The statistical significance of the presence of the counterclockwise disk is low and has been disputed in Yelda et al. (2014). The same authors also do not find the clockwise disks' warp.

Since these studies, the underlying database has grown further. More stars in the GC field have been observed spectroscopically (which is the key to spectral typing and being able to include them in the kinematic analysis). Further, the number of stars for which we can report full orbital solutions has increased due to the longer time coverage. Given these advances and the open questions, we here present a reanalysis of the dynamics of the young stars in the GC.



Original content from this work may be used under the terms of the [Creative Commons Attribution 4.0 licence](#). Any further distribution of this work must maintain attribution to the author(s) and the title of the work, journal citation and DOI.

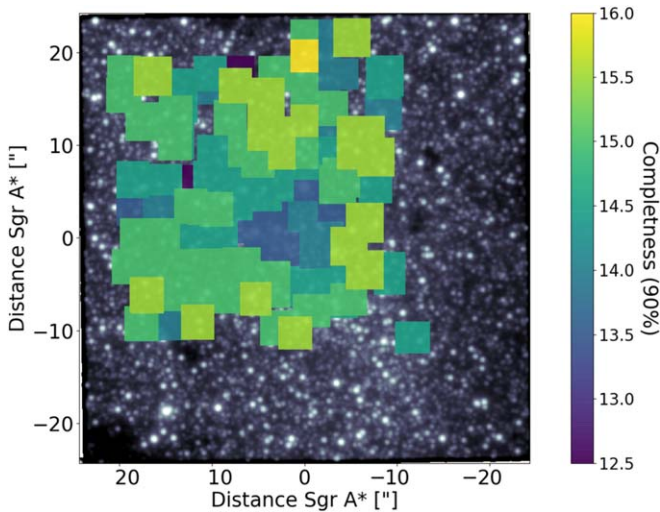


**Figure 1.** 90% completeness estimate based on cross-referencing spectroscopically identified stars with the catalog by Trippe et al. (2008).

## 2. Data Set

### 2.1. Observations

We compile spectroscopic GC observations spanning almost two decades. Our observations consist of adaptive optics (AO)-assisted SINFONI observations, most of which are obtained with the combined  $H + K$  band, with a pixel scale of 100 mas. We reduce and analyze all GC SINFONI pointings. A considerable fraction of these data were analyzed in previous publications (e.g., Paumard et al. 2006; Bartko et al. 2009, 2010; Pfuhl et al. 2011, 2014). Furthermore, we analyze previously unpublished observations of the GC, which were obtained as backup observations of the continuous monitoring of the motions of the stars in the GC (Gillessen et al. 2009, 2017; Gravity Collaboration et al. 2021).

For stars closer than  $2''$  to the black hole, our astrometry is determined from the continuous monitoring program, while for stars at larger projected distances, we rely on the astrometry presented by Trippe et al. (2008) or Fritz et al. (2011) if available. Figure 1 shows an overview of the SINFONI exposures. Our spectroscopic coverage increased substantially compared to previous studies (e.g., Pfuhl et al. 2011; Yelda et al. 2014). While we have reduced the gaps in our coverage, it is biased toward the natural guide star used by the SINFONI AO system in the northeast. Our observations cover a square spanning  $\sim 20''$  to  $\sim -10''$  offset from Sgr A\* in R.A. and  $\sim -10''$  to  $\sim +20''$  in decl. The integration depth across this square is, however, not homogeneous, with some patches suffering from poor quality. Further, bright sources outshine nearby fainter stars in some patches. Only a few southern or northwestern exposures exist, which rely on the laser guide star system (Bonnet et al. 2004). We stack exposures from different epochs if multiple exposures exist. We account for Earth’s motion around the Sun by shifting the wavelength axis of each exposure to the local standard of rest before combination. We try to classify all stars photometrically discernible in the exposures into either young or old type by extracting spectra and identifying the emission and absorption lines. We classify stars as old if the CO-band heads around  $\sim 2.3 \mu\text{m}$  are detected. Young stars are classified by the detection of the Bracket  $\gamma$  ( $\text{Br}\gamma$ ) line at  $2.166 \mu\text{m}$  (and other lines). Because our observations seldom allow for the identification of stars fainter

than  $K_{\text{mag}} = 15$ , such a simple classification scheme suffices to determine the age of the stars (Do et al. 2013). The classification of young stars is complicated by the background  $\text{Br}\gamma$  emission of the ionized gas in the GC, which can mimic young star features in the spectra if the background subtraction is poor. Thus, we allow for stars to remain unclassified if the stars do not show CO-band heads, and the  $\text{Br}\gamma$  line is not credibly detected.

We classified over 2800 stars into unclassifiable, old, or young stars. For all classifiable stars, we determine the radial velocity. In this work, we only investigate the credibly detected young stars and no old stars.

### 2.2. Radial Velocity Measurement of Young Stars

Measuring radial velocities of young stars is complicated by the presence of multiple gas emission clouds that contaminate the  $\text{Br}\gamma$  absorption line of the stars (e.g., Paumard et al. 2006). By selecting a suitable background, we minimize the effect of ionized gas emission. However, this approach is limited. For stars with difficult background subtraction, we revert to the helium absorption line at  $2.113 \mu\text{m}$ , which is less affected by background emission but is significantly harder to detect. This leads to a low signal-to-noise ratio (S/N) in the line detections for many stars. We use line maps to visually confirm stars with faint lines, as well as the consistency of  $\text{Br}\gamma$  and helium velocities. We account for this difficulty by conservatively estimating the uncertainty of the radial velocity. Explicitly, for each star, we obtain three different spectra using three different background aperture masks and determine the radial velocity for each. We determine the radial velocity from the rms of the three spectra, but further increase the derived value if the line is poorly measured. For lines with a discernible helium absorption, we fit a template young star spectrum, otherwise we revert to double- and single-Gauss fits. We checked for consistency of the methods if more than one method was applicable. Further, we check that the derived velocity is different from that of the local ionized gas emission. The mean radial velocity uncertainty is  $58 \text{ km s}^{-1}$ , with many stars having radial velocity uncertainties larger than  $100 \text{ km s}^{-1}$ .

### 2.3. Spectroscopic Completeness

We estimate the fraction of stars we are able to classify. This can be done by planting point sources of different brightness in the images and estimating their detectability. Because our coverage is very patchy and the integration depth is different for each pointing, we revert to a simpler technique: We assume that the catalog by Trippe et al. (2008) is photometrically complete up to  $K_{\text{mag}} = 16$ . Under this assumption, we cross-referenced all stars that we were able to classify as either young or old in this catalog. By binning the catalog stars in steps of 0.5 mag, we can count the fraction of stars we were able to classify spectroscopically. Figure 1 shows the resulting completeness maps. We identify stars up to  $K_{\text{mag}} = 14.5$  for most of our covered area. The central region, which has been observed the most frequently, is less complete than the outer regions. This is a consequence of the increasing number of (bright) stars toward the center. The decreasing number of stars at larger projected distances thus compensates for the shorter integration time. Other than the decreasing completeness in the central region, there is no substantial bias in either the northern,

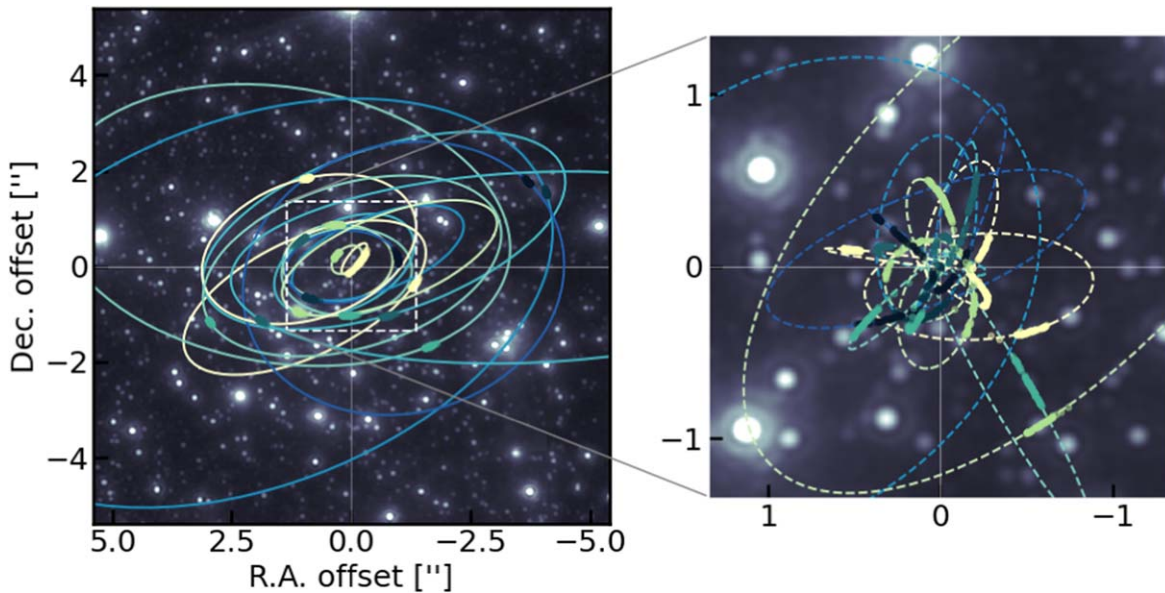


**Figure 2.** Orbits and astrometric measurements of the 36 young stars in the Galactic Center. The track of astrometric measurements is overplotted as darkened points. The orbits of the young stars belonging to the clockwise disk are shown. The inset shows the “Sgr A” star cluster” of the innermost young stars, which are on preferentially eccentric and randomly distributed orbits.

northeastern, or eastern direction, and our completeness estimate is comparable with that found in Pfuhl et al. (2011).

#### 2.4. Stars with Full Orbits

Overall 36 young stars have known full orbital solutions. We give their orbital solutions and uncertainties in Appendix I. Figure 2 shows the inferred orbits. Of these orbits, 31 were presented in previous studies (Gillessen et al. 2009, 2017), but we update their orbital estimates. The procedure for orbit determination is described in detail in these references. Five stars have newly found orbital solutions, which we add here.

#### 2.5. Stars without Orbits

For 159 young stars, we are able to determine five of the six phase-space coordinates  $(x, y, v_x, v_y, v_z)$ , which are given in Appendix J. The total number of known young stars therefore has increased by 79 with respect to Yelda et al. (2014). For several of the known young stars, we updated the radial velocity using the combination of available observations that maximizes the S/N in the spectra. For many stars, this means discarding observations because a given star is affected by hot pixels or other data glitches. In the following, we will describe our star list and compare it with previously published star lists.

#### 2.6. Stars with Radial Velocity from the Literature

For several stars, we resort to previously published values. For instance, we do not reanalyze the radial velocities of any of the Wolf–Rayet stars. For those, the radial velocities need to be derived from a stellar atmosphere model, and the uncertainty is dominated by the modeling and not the S/N of the spectra. Thus, rederived spectra would not improve the radial velocity (F. Martins 2018, private communication). Furthermore, we adopt the radial velocities reported in Yelda et al. (2014) for stars that we either did not observe or when our spectrum is too poor to derive a radial velocity but does not contradict the classification. For stars that are continuously monitored in the

central arcsecond, we either use the radial velocity published in Gillessen et al. (2009, 2017) or an updated value.

#### 2.7. Stars in the Literature Removed from Star List

For five stars reported as young in Yelda et al. (2014) we identified CO-band heads in the spectra. This may be the result of confusion. For instance, our spatial resolution may not suffice to disentangle a young star next to a bright old one. Nevertheless, we remove these stars from our list. We removed the stars S1-19, S4-287, S7-36, S10-34, and S13-3.

### 3. Analysis: Theory and Numerical Experiments

The initial conditions of a test particle in a fixed gravitational potential have six degrees of freedom, corresponding to the initial position and velocity of the particle. It is standard practice to express those in terms of the classical orbital elements: the semimajor axis  $a$ , the eccentricity  $e$ , the inclination  $i$ , the longitude of the pericenter  $\omega$ , the position angle of the ascending node  $\Omega$ , and the epoch of pericenter passage  $t_p$ .

In order to determine these six numbers, one needs to measure six dynamical quantities. From multiepoch astrometry in the GC, one can determine the on-sky position  $(x, y)$  and proper motion  $(v_x, v_y)$  of the object. Thus, one needs two more dynamical quantities in order to determine an orbit. From spectroscopy, one can get the radial velocity of a star  $(v_z)$ . The missing  $z$  coordinate is not accessible directly at the GC distance of  $\sim 8.28$  kpc (Gravity Collaboration et al. 2022), but its absolute value can be determined by measuring acceleration, either by detecting curvature in the on-sky orbital trace or by a change in radial velocity.

For stars with (at least) six dynamical quantities measured, standard fitting techniques uniquely determine the orbital elements; see, for example, Gillessen et al. (2009, 2017). If only five dynamical quantities are known, in almost all cases one lacks an acceleration measurement, i.e., information on  $z$ . Yet, some constraints on the orbital parameters can be

constructed. For example, the angular momentum vector direction can be limited to lie within a one-dimensional half large-circle across the sphere of possible orientations (Paumard et al. 2006; Lu et al. 2009). We call such stars “5D constrained.”

The key finding of earlier works was that when one compares the angular momentum distribution of the 5D-constrained stars, one finds an overdensity in angular momentum in a specific direction. The simplest explanation for that finding is that these stars rotate in a common disk. This interpretation was independently confirmed by stars for which full orbits have been determined (Gillessen et al. 2009; Yelda et al. 2014; Boehle et al. 2016; Gillessen et al. 2017).

The probability distribution of the orbital angular momentum vector for a given star depends on the assumptions one makes on the missing information, i.e., the  $z$  coordinate. Hence, the exact dynamical structure (and thus the significance of certain features such as disks and warps) of the young star sample depends on the choice of the  $z$ -prior.

### 3.1. Determining the Distribution of Angular Momentum Vectors of the 5D-constrained Stars

In order to estimate the smoothed distribution of angular momentum vectors of the 5D-constrained stars, we use the following procedure:

1. Generate 10,000 realizations of each star, where the  $x$ ,  $y$ ,  $v_x$ ,  $v_y$ , and  $v_z$  coordinates are sampled from the respective measured values and errors, assuming Gaussian distributions. The  $z$  coordinate is sampled from the chosen  $z$ -prior distribution, see Section 3.2.
2. Compute the orbital elements corresponding to the phase-space coordinates for each of the 10,000 realizations of each observed star.
3. Like in Yelda et al. (2014), we compute the third-neighbor density of angular momentum vector directions at the desired grid points over the unit sphere spanned by  $(i, \Omega)$  for each of the 10,000 realizations of the sample stars. The neighbor density allows to obtain smooth maps from the discrete distributions.

### 3.2. Constraining the $z$ Values

In the above analysis, one needs to choose what to assume for the distribution of  $z$  values. A natural upper limit on  $|z|$  is obtained by imposing that the orbits need to be bound. This yields a maximum  $z$  value as a function of the projected 2D distance from the massive black hole:

$$|z_{\max}| = \sqrt{\left(\frac{2GM_{\bullet}}{v_x^2 + v_y^2 + v_z^2}\right)^2 - R^2}, \quad (1)$$

where  $R = \sqrt{x^2 + y^2}$  is the 2D projected radius and  $M_{\bullet}$  the mass of the massive black hole. We use this upper limit when sampling the  $z$  coordinate and draw a new  $z$  coordinate in case  $z$  was sampled outside the allowed bounds.

Further, 5D-constrained stars yield an upper limit on the acceleration  $a_{\max}$ . This corresponds to a minimum  $|z|$  value

$$|z_{\min}| = \sqrt{\frac{GM_{\bullet}}{a_{\max}} - R^2}. \quad (2)$$

For the distribution of  $z$  values between the extreme values, two choices have been made in the past:

1. The so-called “stellar cusp prior” (Bartko et al. 2009), which assumes a power-law distribution of  $z$  values, based on the observed power-law density profile of the stellar cusp in the GC (Genzel et al. 2003; Gallego-Cano et al. 2018; Schödel et al. 2018).
2. A “uniform acceleration prior” (Lu et al. 2009; Yelda et al. 2014), where the  $z$  values are computed from a uniform distribution of accelerations.

In Appendix B we show that neither of these priors are ideal in that they do not recover the isotropic structure in the simulated mock data. In order to overcome this problem, we propose a new prior that mitigates the problems of the other two:

1. The “isotropic cluster prior,” which evaluates the probability distribution function of an isotropic cluster for each star. Because the functions for an isotropic cluster are analytically defined, they can be evaluated using the available observational data of each star. The difficulty lies in expressing the distribution function, given in orbital elements, in phase-space coordinates, in which our observations are obtained. We derive the procedure in Section 3.3.

The choice of a certain prior implies choosing the corresponding null hypothesis against which the dynamical structure can be tested. Thus, the choice of prior necessarily introduces some prejudice on what one believes the dynamical structure in GC is.

### 3.3. The Isotropic Cluster Prior

In Appendix A, we described the numerical recipe to sample orbital elements for an isotropic cluster from the respective probability distribution functions (PDFs). Because the PDFs are independent, the combined PDF describing an isotropic cluster is simply the product of the individual distributions:

$$\begin{aligned} \text{PDF}_{\text{iso-clus.}} &= \text{PDF}(a) \cdot \text{PDF}(e) \cdot \text{PDF}(i) \\ &\quad \cdot \text{PDF}(\Omega) \cdot \text{PDF}(\omega) \cdot \text{PDF}(M) \\ &= \frac{p-1}{a_{\min}} \left(\frac{a}{a_{\min}}\right)^{-p} \cdot 2 \sin(i) \\ &\quad \cdot \mathcal{U}_{[0,2\pi]}(\Omega) \cdot \mathcal{U}_{[0,2\pi]}(\omega) \cdot \mathcal{U}_{[0,2\pi]}(M), \end{aligned} \quad (3)$$

where  $\mathcal{U}$  stands for the uniform distribution on the respective interval. We need to express the known distributions of orbital elements as distributions of phase-space coordinates. Effectively, we are thus interested in the correct coordinate transformation of the orbital element distributions to the phase-space coordinate distributions. A probability distribution can be transformed to a different coordinate system by accounting for the volume-filling factor:

$$\text{PDF}_{\text{sys1}} = |\det(\text{Jac})| \cdot \text{PDF}_{\text{sys2}}, \quad (4)$$

where  $\det(\text{Jac})$  stands for the determinant of the Jacobian matrix of the coordinate transformation. In the case of the orbital element coordinate transformation, the Jacobian matrix consists of the 36 partial derivatives of the coordinate transforms. Once the analytical form of the determinant has

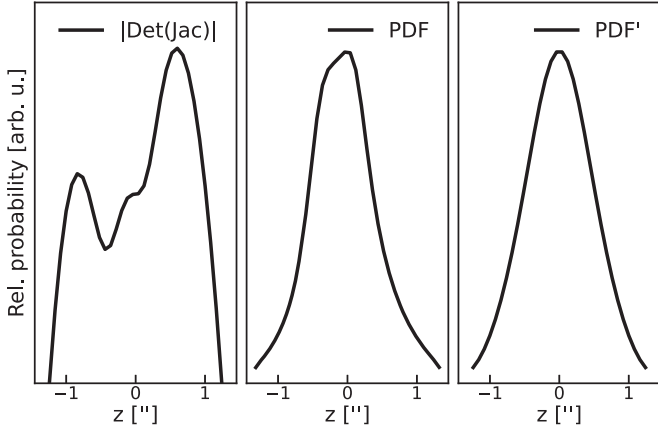


**Figure 3.** Left to right: the determinant of the Jacobian ( $|\det(\text{Jac})|$ ), orbital element probability distribution function ( $\text{PDF}_{\text{iso-clus.}}$ ), and coordinate-transformed probability distribution function ( $\text{PDF}'_{\text{iso-clus.}}$ ) of the star IRS 34W as a function of  $z$  distance. The transformed  $\text{PDF}'_{\text{iso-clus.}}$  is the product of the determinant and the isotropic cluster PDF. Note that the  $y$ -axis for each plot is different.

been determined, we obtain the analytical expression for the  $z$  distribution of stars in an isotropic cluster:

$$\frac{\text{PDF}'_{\text{iso-clus.}}(z|\text{pc}_{\text{obs}})}{\text{PDF}_{\text{iso-clus.}}(a(z|\text{pc}_{\text{obs}}), \dots)} = |\det(\text{Jac}(a(z|\text{pc}_{\text{obs}}), \dots))| \quad (5)$$

where  $\text{pc}_{\text{obs}}$  stands for the observed phase-space coordinates  $x_{\text{obs}}$ ,  $y_{\text{obs}}$ ,  $v_{x\text{obs}}$ ,  $v_{y\text{obs}}$ , and  $v_{z\text{obs}}$ . We implement the determinant in compiled C, which allows very fast evaluation. Figure 3 shows an example of the probability distribution of the  $z$  values for the star IRS 34W (Paumard et al. 2006). Without the determinant, the function is asymmetric; only after multiplication with the determinant is the PDF symmetric around  $z = 0$ .

### 3.4. Significance of Observations

The null hypothesis we test is an isotropic cluster because an old, relaxed distribution should asymptotically reach that state (Bahcall & Wolf 1976; Pfuhl et al. 2011). The procedure to generate an isotropic cluster is described in Schödel et al. (2003) and in Appendix A. Once a mock observation of an isotropic cluster has been generated, we determine its angular momentum distribution the same way as for the real observations outlined in the last section. We use 10,000 mock observations to calculate the mean and standard deviation in each pixel of the  $(i, \Omega)$  map and define the pixel significance  $\sigma_{\text{pixel}}$  as

$$\sigma_{\text{pixel}} = \frac{s_{\text{pixel,obs}} - \langle s_{\text{pixel,sim}} \rangle}{\text{rms}(s_{\text{pixel,sim}})} \quad (6)$$

where  $s_{\text{pixel,obs}}$  stands for the observed pixel value in the  $(i, \Omega)$  map, and  $s_{\text{pixel,sim}}$  stands for the simulated pixel values. This approach is based on the method described in Li & Ma (1983). In Appendix C we show that the derived  $\sigma_{\text{pixel}}$  do not correspond to Gaussian confidence intervals. We use 100,000 mock observations to convert the derived  $\sigma_{\text{pixel}}$  to confidence values and in the following state both values. Note that Yelda et al. (2014) use a different definition of significance based on peak values observed in the  $(i, \Omega)$  maps. We give conversion

estimates between these differently derived significance estimates and discuss the consequences of these different definitions in Appendix C.

## 4. Results: Application to Data

### 4.1. Angular Momentum Distribution of the Young Stars in the Galactic Center

In the following section, we discuss the angular momentum distribution of young stars in the GC. Figure 4 shows the overdensity of angular momentum for six projected radius slices. The density maps are computed using a three-nearest neighbor smoothing (Section 3.1). For stars with determined orbits, we sample 100 realizations of the angular momentum vector from the respective uncertainty estimates. For stars without determined orbits, we sample 100  $z$  values from the isotropic cluster prior and 100 realizations of the measured phase-space vector from the respective uncertainties. We bin our young star samples in six bins with increasing projected distance from the black hole. Table 1 summarizes the structures discussed in the following subsections and states the significance of the features expressed in  $\sigma_{\text{pixel}}$  as well as a confidence limit (see Appendix C for details of the confidence calculation).

#### 4.1.1. The Inner Region

Our updated star sample confirms the presence of a warped clockwise disk for stars in a region ranging from  $\sim 1''$  to  $\sim 4''$  (middle and right plots of the top panel in Figure 4). In this innermost region, most stars are aligned coherently. We call this the inner part of the clockwise disk, abbreviated CW1. For the radial bin ranging from  $2''$  to  $4''$ , CW1 is less dominant and starts to change smoothly to the outer part of the clockwise disk (CW2).

#### 4.1.2. The Intermediate Region

For the radial bin ranging from  $4''$  to  $8''$  (bottom left panel in Figure 4 and Figure 5), no single disk structure dominates the density map. Bartko et al. (2009) and Bartko et al. (2010) found an overdensity for their sample of 30 stars in the range  $3''5$ – $7''$ . They interpret this as a warped extension of the clockwise disk—here called CW2. The significance of the outer part of the warped clockwise disk was estimated at  $\sim 6\sigma$  using the stellar cusp prior (Bartko et al. 2009). However, this outer part was disputed by Yelda et al. (2014). We confirm the CW2 disk at a significance of  $\sim 12\sigma_{\text{pixel}}$ , corresponding to a  $p$ -value of  $p \sim 99.2$  (Figure 5). Further, we find the onset of the counterclockwise feature (CCW/F1) at a significance of  $\sim 10\sigma_{\text{pixel}}$  reported by Genzel et al. (2003), Paumard et al. (2006), and Bartko et al. (2009) in this intermediate region.

#### 4.1.3. The Outer Region

For projected distances larger than  $8''$  we find three prominent features (bottom middle panel in Figure 4 and Figure 6). First, we confirm an overdensity of angular momenta at  $(\phi, \theta) = \sim (0^\circ, 16^\circ)$  significant at  $\sim 35\sigma_{\text{pixel}}$ . This feature was first reported in the outermost radial bin studied by Bartko et al. (2009) and attributed to the clockwise disk. We call this feature outer filament 2 (F2). Second, we find the outer continuation of the CCW/F1 feature with similar significance ( $\sim 35\sigma_{\text{pixel}}$ ). Most prominently, we find a previously unreported feature at

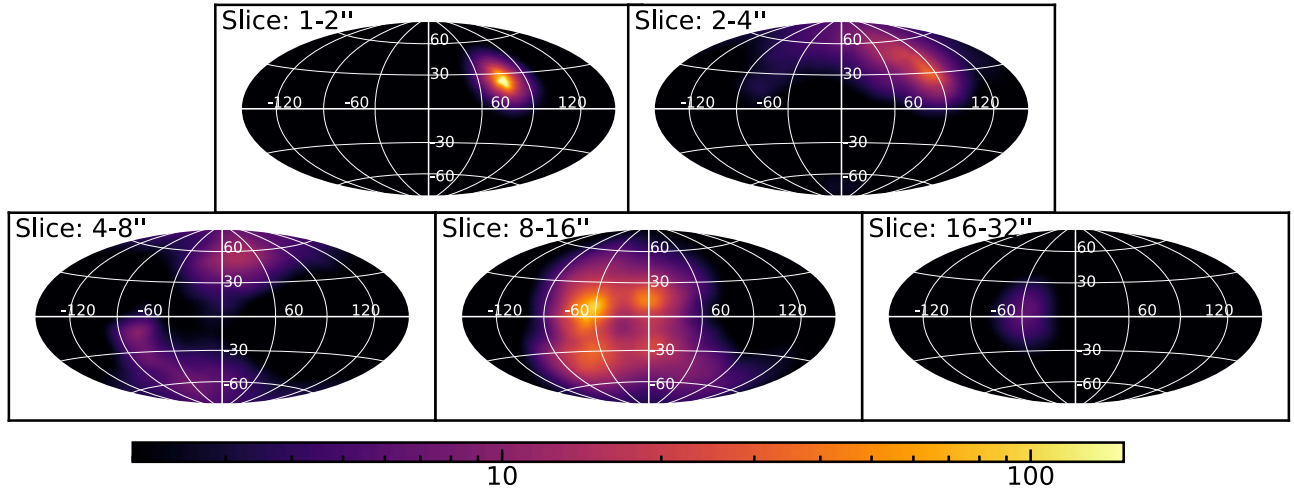


**Figure 4.** Significance ( $\sigma_{\text{pixel}}$ ) of the overdensity of the angular momentum distribution in logarithmic scale as a function of projected radius slice, computed using the isotropic cluster prior. See text for details.

**Table 1**

Angular Momenta Direction, Derived Pixel Significance (Equation (C1)), and the Corresponding Confidence Limits and Gaussian  $\sigma_{\text{Gauss}}$  for the Different Kinematic Features in the Galactic Center

Name	Abb.	$(\theta, \phi)$	$\sigma_{\text{pixel}}$	Approx. Confidence	Approx. Gaussian $\sigma_{\text{Gauss}}$
Inner clockwise disk	CW1	$(73^\circ 1, 34^\circ 5)$	$>100 \sigma_{\text{pixel}}$	$\gg 99.999\%$	$\gg 4 \sigma_{\text{Gauss}}$
Outer clockwise disk	CW2	$(23^\circ 3, 55^\circ 6)$	$\sim 12 \sigma_{\text{pixel}}$	$\sim 99.2\%$	$\sim 2.5 \sigma_{\text{Gauss}}$
Counterclockwise disk/filament	CCW/F1	$(-47^\circ, -30^\circ 0)$	$\sim 35 \sigma_{\text{pixel}}$	$\sim 99.99\%$	$\sim 4 \sigma_{\text{Gauss}}$
Outer filament 2	F2	$(0^\circ 0, 16^\circ 0)$	$\sim 35 \sigma_{\text{pixel}}$	$\sim 99.99\%$	$\sim 4 \sigma_{\text{Gauss}}$
Outer filament 3	F3	$(-44^\circ 2, 11^\circ 5)$	$>100 \sigma_{\text{pixel}}$	$\gg 99.999\%$	$\gg 4 \sigma_{\text{Gauss}}$

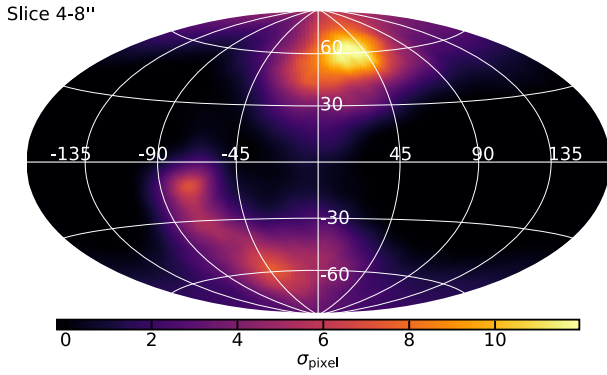


**Figure 5.** Significance ( $\sigma_{\text{pixel}}$ ) of the overdensity of angular momentum for stars at a projected distance from  $4''$  to  $8''$ . The figure is identical to the bottom-leftmost panel of Figure 4, however the color scaling is adapted and in linear scale.

$(\phi, \theta) = \sim (-44^\circ, 12^\circ)$  at a very high significance of  $>100\sigma_{\text{pixel}}$ . We call this feature the second outer filament—F3.

The location and significance of all these overdensity features is tabulated in Table 1.

## 5. Results: Estimating the Disk Membership Fraction

In order to assess the disk membership of each star in one of the features, we numerically integrate the star's PDF to calculate the Bayesian evidence. We do so using the statistical software package *dynesty* (Skilling 2004, 2006; Speagle 2020). We sample the likelihood function in phase-space coordinates, which allows sampling only the allowed part of the phase space

and includes the prior information on the feature location as an additional term in the likelihood function  $L_{\text{feat}}$ , which is a Gaussian prior with a specified width at the feature location. We do not impose other prior knowledge on the stars other than the disk location, and thus we assume a flat prior on the  $z$  coordinate of each star, constrained only by the maximum  $z$  distance allowed for a bound orbit. Further, we assume a flat prior on the remaining phase-space coordinates with width equal to four times the standard deviation of each coordinate expectation value. In contrast to the isotropic cluster prior used in Section 3.2, the volume element is numerically derived by the evaluation of the likelihood function by *dynesty*. Explicitly, we integrate the following likelihood function:

$$\begin{aligned}
 \log L_{\text{model}} &= \log L_{\text{feat}} + \log L_{\text{star}} \\
 &= -0.5 \left( d(i_{\text{feat}}, \Omega_{\text{feat}}, i(x, \dots), \Omega(x, \dots))^2 / \sigma_{\text{feat}}^2 \right. \\
 &\quad \left. + \sum_n (x_{n,\text{obs}} - x_i)^2 / \sigma_{x_{n,\text{obs}}}^2 \right),
 \end{aligned} \tag{7}$$

where  $d(i_{\text{feat}}, \Omega_{\text{feat}}, i(x, \dots), \Omega(x, \dots))$  stands for the spherical cap distance<sup>11</sup> from the feature angular location  $(i_{\text{feat}}, \Omega_{\text{feat}})$ , computed for each sample of the phase-space coordinates  $(x, y, z, v_x, v_y, v_z)$ .  $\sigma_{\text{feat}}$  is the opening angle of the feature, which we set to  $20^\circ$  for all features. We illustrate the feature priors in Figure 7.

<sup>11</sup> That is, the Haversine distance.

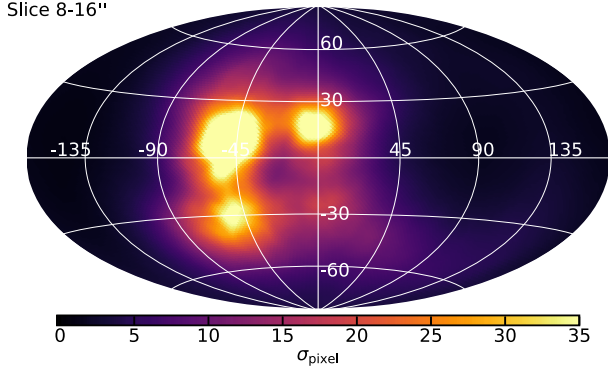


**Figure 6.** Same as Figure 5, projected distance from 8'' to 16'', again with adapted color scaling and in linear scale.

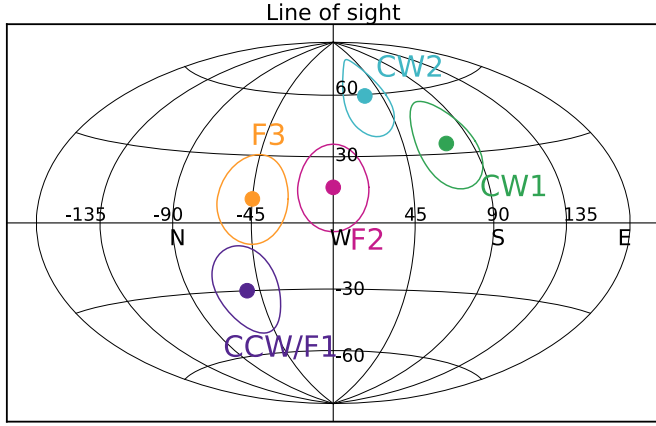


**Figure 7.** Illustration of the location and width of the feature priors assumed, tabulated in Table 1.

Similarly, we can define the likelihood of a star without the disk prior:

$$\log L_{\text{star}} = \sum_i (x_{i,\text{obs}} - x_i)^2 / \sigma_{x_i}^2. \quad (8)$$

Because we integrate the same phase-space ( $pc$ ) prior volume for each star, the log evidence evaluates to the same value  $\int \log L_{\text{star}} dpc = -5.8$  for each star. For stars with orbital solutions, it suffices to sample  $i$  and  $\Omega$ . Equation (7) thus can be rewritten as

$$\begin{aligned} \log L_{\text{model}} &= \log L_{\text{feat}} + \log L_{\text{star}} \\ &= -0.5 \times (d(i_{\text{feat}}, \Omega_{\text{feat}}, i, \Omega))^2 / \sigma_{\text{feat}}^2 \\ &\quad + (i_{\text{obs}} - i)^2 / \sigma_{i_{\text{obs}}}^2 + (\Omega_{\text{obs}} - \Omega)^2 / \sigma_{\Omega_{\text{obs}}}^2, \end{aligned} \quad (9)$$

The corresponding integral to Equation (8) for the stars with determined orbits evaluates to a log evidence of  $\sim -2.3$ .

By comparing the log evidence of  $L_{\text{model}}$  with the log evidence  $L_{\text{star}}$ , we can compare the feature membership probability for stars with and without orbital solutions. In order to establish feature membership, we require the difference of the log evidence  $L_{\text{model}} - L_{\text{star}}$  to be smaller than 2. Essentially, our procedure corresponds to a log-likelihood cut. However, it can be viewed from a Bayesian model selection point of view where one compares evidence ratios: If the relative log evidence of  $L_{\text{star}}$  and  $L_{\text{model}}$  is smaller than 2, the star is consistent with belonging to the respective feature.

**Table 2**

Significant Kinematic Features of the Young Star Population in the Galactic Center

Disk Name	Number of Stars	Brighter/ Fainter than $K_{\text{mag}} = 14$	IQR Semimajor Axes	IQR Eccentricity
CW1	33	24/9 = 2.7	1''6, 2''1, 2''7	0.4, 0.5, 0.6
CW2	13	12/2 = 6	5''8, 7''0, 8''5	0.2, 0.4, 0.5
CCW/F1	33	21/12 = 1.8	5''4, 7''4, 12''1	0.4, 0.5, 0.6
F2	37	23/8 = 2.8	2''2, 5''6, 9''3	0.4, 0.6, 0.9
F3	36	20/16 = 1.3	3''7, 8''8, 12''4	0.6, 0.7, 0.9

**Note.** Number of stars, luminosity, semimajor axis, and eccentricity distribution. The number counts of stars are the observed values, i.e., no completeness correction is applied.

Tables 6 and 8 report stars consistent with belonging to the CW1 and CW2, Table 7 reports the stars consistent with belonging to the CCW/F1, and Tables 9 and 10 reports the stars consistent with being on the F2 and F3 features.

### 5.1. Is it Necessary to Debias the Disk Fraction?

Yelda et al. (2014) estimated the true disk fraction by comparing the observed distribution against their simulations of an (approximate) isotropic cluster mixed with a stellar disk. This approach is correct under the assumption that the young stars not aligned with the disk are in an isotropic distribution. If the distribution of the not-aligned stars is anisotropic, for instance if several streams of stars exist, this approach underestimates the number of disk members. We thus do not estimate the true disk fraction under the assumption of a single disk + isotropic cluster model. Consequently, we cannot tell the difference between a star aligned by chance and that of a true feature member. Our feature fraction estimate is 100%, which should be understood as an upper limit. Further, we impose that each star is at most a member of one feature. If a star could be associated with more than one feature, we count it to the feature with the lowest  $\Delta$  evidence.

Ultimately, our feature membership depends on the prior width and location of the features and the evidence cut. Optimally, these feature properties should be inferred from the data, too, which however requires a hierarchical approach that is beyond the scope of this work.

## 6. Results: Properties of the Young Stellar Components

Marginalizing the prior and likelihood functions in Equation (7), we obtain posterior phase-space distributions for each star. For the stars that satisfy our feature membership criterion, we compute the orbital elements and obtain the posterior density estimate of the orbital elements. Because all stars are independent of one another, we can combine the posterior estimates from each sample and obtain the joint orbital element distribution.

In the following, we analyze the posterior semimajor axes and eccentricity distributions as well as their luminosity distributions. In this discussion, we only touch on the prior on the preferred direction of angular momenta and our observational data (Table 2). We do not require stars to have certain projected distances or eccentricities. However, we require that all stars belong to at most one feature. Further we

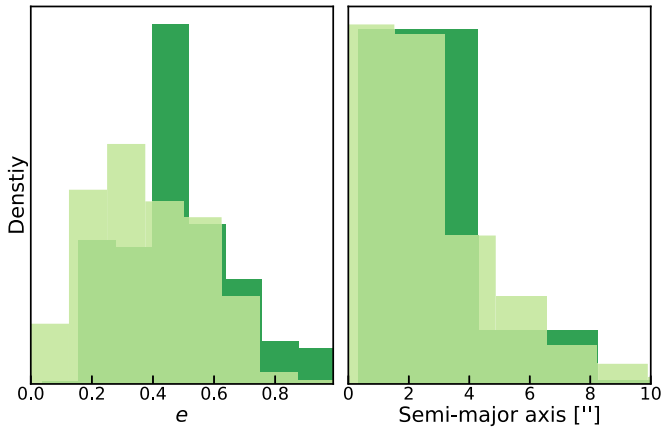


**Figure 8.** Distribution of the eccentricity and the semimajor axis of the stars consistent with belonging to the inner part of the warped clockwise disk. The dark green histograms show the properties of the 5D-constrained stars, and the light green histogram show the distribution of stars with determined orbital solutions. The gray and black vertical lines indicate the median, and the dashed lines indicate the IQR of the stars with and without orbit.

remove B-type stars that lie within  $0''.8$  of Sgr A\*. These so-called S stars have a relaxed angular momentum distribution (e.g., Gillessen et al. 2017), thus we assume that their alignment with any of the features is by chance. In the following, observed number counts and summary statistics will be presented, without the inclusion of a completeness correction.

### 6.1. The Warped Clockwise Disk and Its Stars

Our updated star sample confirms the presence of a warped clockwise disk. We do not model the clockwise disk with a “warp”, i.e., a smooth change of angular momentum. Instead, we define two angular momentum directions motivated from the observed overdensities of angular momentum compared to an isotropic cluster (see Figure 4 and Table 1). This allows us to check if stars consistent with belonging to the respective features are indeed similar to one another, without imposing the “warpedness” already in the prior.

We find 33 stars that are consistent with being in the CW1 disk. Only four stars are at a projected distance greater than  $4''$ , with the largest projected distance being  $\sim 10''$ . The median projected distance is  $2''.0$ , the interquartile range (IQR) of the clockwise disk feature stars is  $1''.0$  and  $3''.2$ . The majority of the clockwise disk stars are bright: 24 of the 33 stars are brighter than  $K_{\text{mag}} = 14$ . Nevertheless, there is no distinctive brightness cut that leads to disk membership: nine stars are fainter than  $K_{\text{mag}} = 14$ , six of which have determined orbital solutions (R1, S5, S11, S31, S66, and S87). The median  $K_{\text{mag}}$  of the clockwise disk is 12.7.

Combining the posteriors, we obtain the joint distribution of orbital elements. For stars with determined orbital solutions, we sample orbital elements from the respective orbit posterior distributions. Figure 8 plots the distribution of the eccentricities and the semimajor axes. The stars without determined orbits typically have nonzero eccentricities, with a median eccentricity of  $\sim 0.5$ ; highly eccentric orbits are however not preferred by our data. The median semimajor axis is  $2''.1$ . The distribution of the stars with determined orbital solutions broadly agrees with those without a fully determined orbit. The stars with determined orbital solutions have however slightly lower eccentricities, and very high eccentricities are completely suppressed.

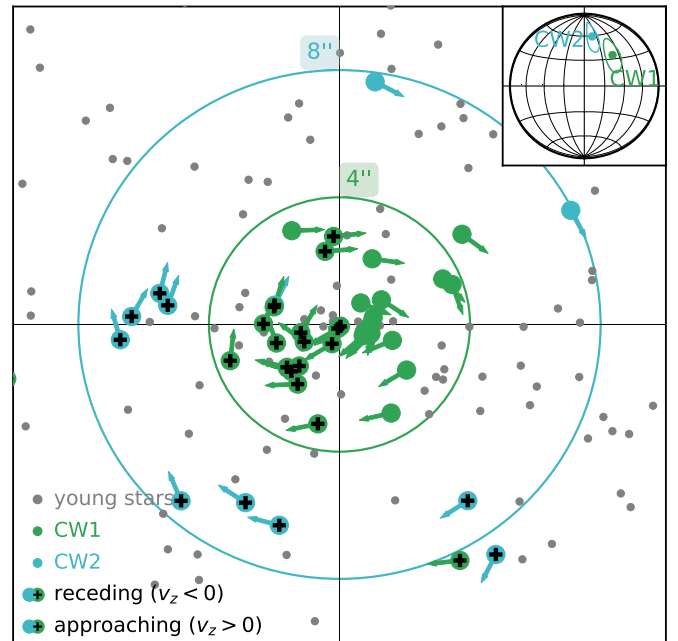


**Figure 9.** Comparison of stars belonging to the CW1 (green) and CW2 (blue) disks. Stars that do not belong to either feature are plotted in gray. The inset shows the prior width and direction of the feature prior  $L_{\text{feat}}$  based on which the colored stars are selected (i.e.,  $\Delta \log \text{evidence} > 2$ , Section 5). Stars marked with a “plus” have positive radial velocity, unmarked stars have a negative radial velocity. The arrows indicate the direction of the projected velocity. In both cases we evaluate the disk membership probability for all young stars, i.e., no radial binning has been applied.

In summary, the CW1 disk is made up of predominantly, but not exclusively, O/WR-type stars, on eccentric orbits in the proximity of the black hole.

Thirteen stars are consistent with belonging to the CW2 disk. All but two stars are brighter than  $K_{\text{mag}} = 14$ . One faint star is S60 and belongs to the S-star cluster, so we remove it from the sample. The median magnitude is 12.7. All but one star have projected distances ranging between  $4''$  and  $\sim 8''.6$ , the median projected distance is  $\sim 6''.6$ .

The eccentricity distribution is comparable to the eccentricity distribution of the CW1 disk, with a median eccentricity of  $\sim 0.4$ ; high eccentricities are not favored by our data, and the median semimajor axis is  $7''.0$ . The star R70 has a determined orbital solution with a semimajor axis of  $\sim 3''.5$  and an eccentricity of 0.3, consistent with the 5D-constrained stars.

In summary, the CW2 disk consists of 11 O/WR stars and 1 B star on slightly eccentric orbits. The stars are bright, very similar to the CW1 stars, but are found at larger radii.

Figure 9 demonstrates the morphological difference between the inner and the outer parts of the warped clockwise disk. All but three stars belonging to the inner part of the disk are found centralized within  $5''$ . The stars in the outer part are thus only different by their angular momentum direction as a function of radius. This is consistent with a “warp picture,” which is solely the result of the data and not the prior. The feature prior  $L_{\text{feat}}$  does not impose a radial dependence or a magnitude selection.

### 6.2. The CCW/F1 Feature and Its Stars

Thirty-three stars are consistent with belonging to the CCW/F1 feature (Figure 10, right). Only two stars, S4 and S12, have full orbital solutions, both of which are S stars, which we again discard. Twelve stars are brighter than  $K_{\text{mag}} = 14$ , 21 are



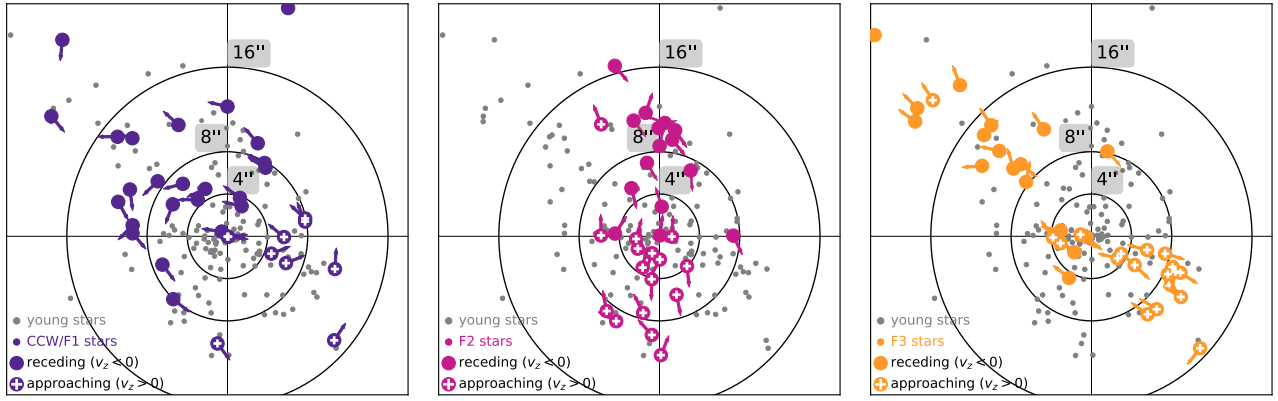


Figure 10. Same as Figure 9 for CCW/F1 (purple), F2 (pink), and F3 (orange).

fainter, and the feature is therefore more skewed toward fainter, B-type stars, compared to the clockwise disk. The median magnitude is 13.5. This feature contains stars mostly at large projected distance, with a median projected distance of  $8''.0$ .

The stars are on modestly eccentric orbits, with a median eccentricity of 0.5. Unlike for the CW1/2 features, highly eccentric orbits are not entirely suppressed. However, the fraction of the CCW/F1 stars on highly eccentric orbits (eccentricity  $>0.9$ ) is small. The semimajor axes distribution is similar to the observed projected distances, with a median semimajor axes of  $7''.4$ .

### 6.3. The F2 Feature and Its Stars

Thirty-seven stars are consistent with belonging to the F2 feature (Figure 10, middle). Similar to the CW disk, the majority of stars are brighter than  $K_{\text{mag}} = 14$ : 8 stars are fainter, 23 brighter. The median magnitude is 13.2. The stars are at a median projected distance of  $7''.0$ .

The median eccentricity is 0.7, higher than for the CW disk and the median of semimajor axes is  $5''.6$ .

### 6.4. The F3 Feature and Its Stars

The F3 feature consists of 36 stars (Figure 10, left). Two stars have a full orbital solution, which, however, belong to the S-star cluster. Two-thirds of the stars belonging to this feature are brighter than  $K_{\text{mag}} = 14$  (16 B-type stars, 20 O/WR-type stars). As for the CCW disk, the stars are at large projected distances: The median distance is  $8''.8$ .

Most of the F3 stars are preferentially on highly eccentric orbits, which differentiate the F3 feature from the other features. Indication for such almost radial orbits have already been reported in Madigan et al. (2014). The median eccentricity is 0.7. The distribution of semimajor axes is comparable to the observed projected distances with median 7.8. Intriguingly, the orientation of the F3 feature is in the same plane as the galaxy; however, the sense of rotation is opposite it (Paumard et al. 2006).

### 6.5. K-band Luminosity Function of the Young Stars

Following Bartko et al. (2010), we define the K-band luminosity function (KLF) as

$$KLF(R_1, R_2, m_K) = \frac{N_{\text{stars,obs}}(R_1, R_2, m_K)}{A_{\text{eff}}(R_1, R_2, m_K)}, \quad (10)$$

where  $N_{\text{stars,obs}}$  is the number of observed stars in the radial slice ( $R_1, R_2$ ) and magnitude bin  $m_K$ , and  $A_{\text{eff}}$  is the effective

area in the radial and magnitude bin. If our observations were perfect, the effective area would simply depend on the radial slice. However, our spectroscopic integration depth varies from pointing to pointing, and our classification fidelity strongly depends on the background gas emission and the presence of bright stars. Thus, we have to take the completeness of our observations into account, and the effective area is computed as

$$A_{\text{eff}}(R_1, R_2, m_K) = \iint_{\sqrt{x^2+y^2} \geq R_1}^{\sqrt{x^2+y^2} \leq R_2} \epsilon(x, y, m_K) dx, dy. \quad (11)$$

We compute the completeness similar to Do et al. (2013), comparing the number of photometrically identified stars present in a given SINFONI pointing, with the number of stars we were able to classify spectroscopically. This method allows the much better photometric information of a star to be exploited.

Explicitly, we use the star catalog presented in Trippe et al. (2008) and assume it to be complete to  $K_{\text{mag}} = 16$ . Then, for each pointing, we calculate the ratio of spectroscopically classified stars to the total number of stars:

$$\epsilon(x_{\text{pointing}}, y_{\text{pointing}}, m_K) = 1 - \frac{N_{\text{unclassified}}(m_K)}{N_{\text{total}}(m_K)}. \quad (12)$$

We assess the uncertainty of the completeness correction by simulating different completeness maps based on the number of classified and unclassified stars. We detail the procedure in Appendix E.

We compare the KLF found in our work with the ones found by Do et al. (2013) and Bartko et al. (2010) in Appendix F. Overall, the agreement between our values and those found in Bartko et al. (2010) is good, despite using a different method for determining the completeness correction. In contrast to Do et al. (2013), we do not infer the completeness-corrected KLF and completeness correction simultaneously but calculate it from the star counts once the completeness of each pointing is determined. The most important difference to Do et al. (2013) is that we do not enforce classification into either young or old, but allow a star to remain unclassified. Consequently, we do not differentiate young and old star completeness but simply calculate the fraction of classified and unclassified stars. This prevents stars with no signal in the spectrum from being classified, and thus conservatively estimates the completeness. The completeness correction is nonnegligible for deriving the

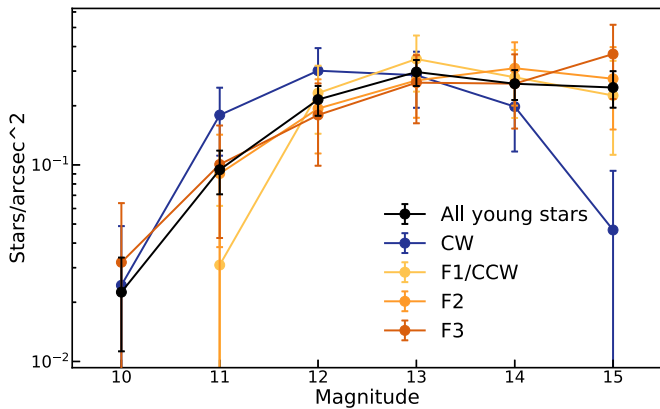


**Figure 11.** KLFs of stars associated with the different kinematic features and the KLF of all young stars including the central S stars. No explicit projected radius cut is applied, but we combine the stars of clockwise disk (CW1 and CW2).

KLF. For instance, the overall completeness in the  $K_{\text{mag}} = 13.5$  to  $K_{\text{mag}} = 14.5$  bin is on the order of 56%.

In order to assess whether the higher O+WR to B star ratio of the CW disk and the other kinematic features is an artifact of the incomplete observations, we plot the completeness-corrected KLF of the stars associated with the respective features as well as the KLF of the all young stars combined (including the central young S stars) in Figure 11. The KLFs of the outer features are essentially indistinguishable, while the KLF of the warped clockwise disk peaks at  $K_{\text{mag}} = 12$  and is thus top heavy. The overall KLF follows those of the outer features, as those dominate the star count.

### 6.6. Summary of the Young Stellar Components

This analysis has revealed that the young stars can be categorized into five different significant features. As many as 75% of the young stars (152 of 201) are consistent with belonging to one of these features. Our analysis has shown that these features cannot only be separated by their angular momentum but also by their distance from Sgr A\*. The CW disk forms a coherent structure ranging from  $\sim 1''$  to  $\sim 8''$ . The F2 feature has a large range from  $\sim 3''$  to  $\sim 10''$ . The CCW/F1 and F2 features extend the farthest from Sgr A\*. We compare the different eccentricity distributions, semimajor axis distributions, and the  $K_{\text{mag}}$  distributions in the Appendix D (Figure 18).

## 7. Discussion

We carried out a spectroscopic survey of the central ( $+20''$ ,  $-10''$ ), ( $-20''$ ,  $+10''$ ) of the GC. We reanalyzed, combined, and updated the spectra derived for all GC stars observed with ESO’s SINFONI instrument taken in AO mode. This led to spectra for over 2800 stars. We classified the stars as old, if CO-band heads are discernible; young, if the Br $\gamma$  lines (and other young star lines) are discernible; or unclassifiable, if no line is discernible. This led to the identification of a total of 201 young stars. For 35 young stars, full orbital solutions can be derived. Three stars have too high radial velocities to be on bound orbits.<sup>12</sup> For the remaining 158 stars, only radial velocities could be determined. We extend previous Monte Carlo studies presented in Lu et al. (2009), Bartko et al.

<sup>12</sup> This is likely a consequence of a poorly determined radial velocity or a confusion event.

(2009, 2010), and Yelda et al. (2014) by introducing a new prior. The proposed prior maps an isotropic cluster onto itself without bias in angular momentum. It is not “better” for answering the question of the true angular momentum distribution of the young stars. However, it allows for a clean definition of a null hypothesis: how different is the observed distribution from an isotropic cluster. In particular, we ask how different the observed angular momentum distribution is from that of the old star cluster present in the GC, which is an isotropic cluster to good approximation (e.g., Pfuhl et al. 2014).

### 7.1. Distribution of Angular Momentum of Young Stars in the Galactic Center

We find five significantly different kinematic features compared to an isotropic cluster. Further, we have found that the vast majority (75%) of stars can be attributed to one of these five features. The angular momentum distribution in the GC is therefore very rich and significantly different from the old star population. We demonstrate that the young stars reside in a warped disk and several outer filaments. Such a rich structure has been proposed by several simulations of in situ star formation in an infalling gas cloud scenario. Bonnell & Rice (2008) demonstrated that stars can form in massive gas clouds around a massive black hole like Sgr A\* and speculated that multiple young star rings may be present in the GC. Löckmann & Baumgardt (2009) have demonstrated that in the presence of two separate disk systems (like the clockwise and the counterclockwise system), the disks tidally interact with one another, causing warping of the disks. Further, Kocsis & Tremaine (2011) show that warping of the disk naturally arises from the interaction of the disk with the potential of the embedding old star cluster. Our observations are fully consistent with the results of these simulations and theoretical arguments.

### 7.2. K-band Luminosity Function

Figure 19 and Figure 11 show the KLF of the young stars within  $1''$  to  $12''$  and the KLFs of the kinematic components. The KLF derived from our revised sample of young stars and revised completeness correction is consistent with the KLF reported in Bartko et al. (2010). Compared to Bartko et al. (2009), who used source implanting to derive the completeness, and following Do et al. (2013), we use the information available in photometric observations of the GC to improve the completeness correction. Nevertheless, the KLF derived here is more top heavy than the one in Do et al. (2013).

Comparing the KLFs of the different kinematic features we find that the combined KLFs of the CW1 and CW2 features are more top heavy than that of the other features. The KLFs of the outer features are comparable to the KLF of the inner S-star cluster and the young stars at large separations reported in Bartko et al. (2009) and are thus consistent with a normal Salpeter/Kroupa IMF (Salpeter 1955; Kroupa 2001) of  $dN/dm \propto m^{-2.15}$ . Nevertheless, the statistical significance of this result is low. For instance, the  $p$ -value of the K-S test between the CW disk KLF and the CCW/F1 feature is 0.23, yielding only marginal evidence that these distributions are different. If one combines the three outer features, the significance is increased ( $p$ -value 0.03). Thus, we caution that this result remains tentative and that the decisive magnitude bin to confirm the downtick of the warped clockwise disk KLF is

stars fainter than  $K_{\text{mag}} = 15$  and thus beyond the fidelity of this work.

Assuming the difference is not an artifact of the completeness correction, two possibilities emerge. If star formation is universally top heavy in the GC, the absence of brighter stars may be the result of the main-sequence cutoff. This would imply that the outer structures are older and bear witness to star formation events prior to the formation of the clockwise disk stars. Alternatively, the IMF in an accreting gas cloud may be radially dependent, and the observed KLF could thus be explained in a singular star formation event.

### 7.3. A Warped Disk and Several Filaments of Young Stars

In Section 6 we show that the CW disk forms a coherent structure ranging from  $1''$  to  $8''$ . The stars share very similar eccentricities, have similar angular momentum directions, and are predominantly made up of O- and WR-type stars. They are mainly differentiated by the angular momentum as a function of separation from the black hole, consistent with the warp picture. The other features are harder to explain as an extension or warp of the clockwise disk.

The CCW/F1 feature possesses a similar eccentricity distribution to the two inner features but shows a drastically different angular momentum direction.

The F2 feature shares some similarities with the CW disk and could thus be its outermost extension. For instance, some of the F2 stars have low eccentricities. However, many of the F2 stars have higher eccentricities atypical for the CW disk stars.

The F3 feature has a different angular momentum direction than the warped clockwise disk, which is not too different from that of the CCW/F1 feature. It is the most eccentric feature.

Ultimately, all three outer features share a very similar  $K$ -band luminosity function, which appears to be different from the one of the CW disk.

Several simulations of the gas accretion disk produced such rich features (Nayakshin 2006; Nayakshin et al. 2007; Bonnell & Rice 2008; Löckmann & Baumgardt 2009). Of particular interest is the scenario that was studied in Hobbs & Nayakshin (2009), in which two Giant Molecular Clouds collide. After the initial collision, the two clouds are sent on a plunging orbit and accrete onto Sgr A\*. A central accretion disk and, depending on the initial conditions, several gas streamers form. In both the central disk and the gas streamers, stars subsequently form.

Several of the predictions made in this scenario are consistent with our observations. In the simulations with large impact parameters, the innermost accretion disk stays in a rather compact region around the black hole, consistent with the inner region of the CW disk in the GC. The remnants of the colliding gas clouds form filaments at larger separations, which do not share the same angular momentum direction as the central disk. This could correspond to the stellar populations found in the CCW/F1, F2, and F3 features. Furthermore, the disks found in the simulations show large-scale warps, perfectly consistent with the observed change in the angular momentum direction of the CW disk. In these simulations, the central disk circularizes after an initial period of highly eccentric orbits, while the stars farther out remain on more eccentric orbits. We find a similar behavior, but note that our values are overall more eccentric than found in this set of simulations.

In the simulations, the star formation is different in the inner and outer regions. While Hobbs & Nayakshin (2009) caution that their star formation prescription may be oversimplified, in their simulations, mostly heavy stars form in the central disk and the IMF is substantially less top heavy in the outer filaments. This is consistent with our observations, too: The ratio of observed O+WR to B stars is much higher in the warped clockwise disk than in the outer structures. Our data confirm that while the KLFs of the outer structures are indistinguishable, the KLF of the warped clockwise disks peaks at  $K_{\text{mag}} = 12$ , and stars fainter than  $K_{\text{mag}} = 14$  are rare.

While matching the observations well, the effect of the embedding old nuclear star cluster is typically ignored in such simulations of star formation. However, through the process of vector resonant relaxation, the embedding old star cluster facilitates a fast reorientation of the angular momentum direction. This process can lead to a warping of initially coherent disk-like structures in timescales comparable to the age of the young stars (Kocsis & Tremaine 2011) and can lead to clustering in angular momentum space for stars of different mass (Szölgény & Kocsis 2018). For an isotropic background potential, the timescale at which an initially coherent structure is dissolved increases with separation from the center (Kocsis & Tremaine 2015), and the existence of the clockwise disk structure constrains the efficiency of vector resonant relaxation processes in the Galactic Center (Giral Martínez et al. 2020). It is thus not clear if the observed structure can be explained solely by the effect of the embedding cluster.

Another intriguing aspect of the young star population is the central S-star cluster: The central  $0''8$  of the Galactic Center is populated by B-type stars, with an approximately isotropic angular momentum distribution and a superthermal eccentricity distribution (Gillessen et al. 2009; Boehle et al. 2016; Gillessen et al. 2017). The very different angular momentum distribution and the evident absence of any WR- and O-type stars on tight orbits pose a significant complication of the physical picture for the formation of these young stars. One solution is presented in Chen & Amaro-Seoane (2014), who propose a so-called rapidly evolving region (RER) in the inner region of the clockwise disk. If the initial disk is sufficiently heavy, stars within the RER rapidly exchange eccentricity and semimajor axis through Kozai–Lidov-like resonances. This reorients the orbits into the observed superthermal, isotropic distribution. The presence of the outer filaments may be indicative that enough initial mass was present for such an RER to form. Further, this scenario can also explain the absence of WR- and O-type stars in the central region, as those stars migrate close enough toward the black hole to be tidally disrupted. If the central S-star cluster would belong to the same dynamical component as the CW disk stars, the number of fainter B-type stars is increased, altering the KLF of this feature. We discuss this possibility in Appendix G.

Nevertheless, the strict isotropy of the angular momentum has been challenged by Ali et al. (2020), who report two planes of resonances,<sup>13</sup> with an apparent overdensity in the orbital inclination of both the late- and early-type stars in the central arcsecond. Our analysis provides an appropriate tool to measure the anisotropy of an observed stellar distribution by comparing it against an isotropic cluster. We could not confirm

<sup>13</sup> Note that Ali et al. (2020) refer to the plane of orbits as a “disk.” However, the stars in their “disks” show both clock and counterclockwise rotation, which is inconsistent with our nomenclature.

a significant anisotropy in the central region other than in the direction of the clockwise disk (see Appendix H for details). However, we did not include late-type stars, which contribute to their findings. In addition, our test is more constraining as it requires isotropy in all orbital elements, rather than just in the orbital inclination. Thus, we cannot rule out that such planes exist.

Lastly, the observed young stars might not have formed together at all. The main-sequence lifetime of B stars is much longer than that of the O and WR stars, and further star formation in the Galactic Center has been shown to be episodic with evidence of star formation in recent history ( $\sim 100$  Myr) (Pfuhl et al. 2014; Schödel et al. 2020). The study of the age distribution of the bright young stars in the CW and CCW features has, however, not revealed a secondary star formation event (Bartko et al. 2010; Lu et al. 2013). Madigan et al. (2014) discuss a scenario in which older B stars (60–100 Myr) interact with the potential of the black hole, the isotropic old star cluster, and the CW disk. In this scenario binary stars are placed on near radial orbits with very high eccentricities due to the interaction with massive perturbers (Perets et al. 2009; Perets & Gualandris 2010). After some time the binary is disrupted and one partner is captured in a tight orbit around the black hole. This scenario could thus explain the high-eccentricity orbits observed for the F3 feature, implying that F3 stars correspond to the stars found in the magnitude bin  $K_{\text{mag}} > 15$  of Madigan et al. (2014). Conveniently, this scenario explains the B stars found in the innermost region around Sgr A\*, which however seem to have similar ages to the CW disk stars (Habibi et al. 2017).

## 8. Conclusion

We confirm the presence of a warped clockwise disk (Bartko et al. 2009, 2010): it exhibits a smooth change in angular momentum as a function of radius. We confirm the presence of an outer kinematic feature (F2), which Bartko et al. (2009) attributed to the CW disk. The feature shares similarities to the CW disk, but also to the features at larger separations. We associate it with the other outer structures but note that it remains possible that it is part of the CW disk. Further, we confirm the presence of a counterclockwise feature at large separations reported in Genzel et al. (2003), Paumard et al. (2006), and Bartko et al. (2009). This feature was deemed insignificant by other works: Lu et al. (2006), Lu et al. (2009), and Yelda et al. (2014). We find that this feature consists mostly of stars at large projected separations, explaining the difficulty of establishing significance in past studies that had smaller spatial coverage. In addition to the features that have been discussed in the literature before, we identify a new feature, F3, which, like the CCW/F1 and F2 features, is at large projected distances from the black hole. The F3 feature is, however, substantially more eccentric, and we thus argue that the systems are distinct.

This rich structure in kinematic features has been suggested in different simulations of star formation in an accretion disk around Sgr A\*. The set of simulations by Hobbs & Nayakshin

(2009) in which two giant molecular clouds collide and subsequently accrete show intriguingly comparable features to the ones observed: A small, medium eccentric disk in close proximity to Sgr A\*; several remnant star streamers at larger separation, which have substantially different angular momenta directions; and higher eccentricities at larger separations. Further, the simulations show differences in the distribution of O- and WR-type stars, with the heaviest stars found in the inner disk—consistent with the apparent distribution of O- and WR-type stars in the GC. We thus argue that the simultaneous formation of all young stars in the GC remains a feasible scenario, consistent with the latest analysis of the age distribution of the S-star cluster (Habibi et al. 2017). However, the dramatically different kinematic distribution of B stars in the central arcsecond remains a serious challenge (Boehle et al. 2016; Gillessen et al. 2017) for such a common formation scenario, and a more detailed analysis of the age distribution of the young stars is required to confirm or rule out a single star formation event some  $\sim 6$  Myr ago.

We thank the referee for a very quick yet thorough report, which helped to improve the paper. A.D., S.V.F., and F.W. acknowledge support from the Max Planck International Research School.

## Appendix A Generation of Mock Isotropic Cluster

The procedure to generate mock observations of an isotropic cluster is adapted from Schödel et al. (2003):

1. Sample the inclination  $i$  and the longitude of the ascending node  $\Omega$  isotropically on a sphere.
2. Sample the argument of pericenter uniformly from  $\omega \in [0^\circ, 360^\circ]$ .
3. Draw the semimajor axis from a power-law distribution  $\frac{dN}{da} \propto a^{-\beta}$ . We choose  $\beta=2$  to resemble the observed distribution of stars. We sample  $a$  from  $0''.2$  to  $40''$ , in order to match the observed scales.
4. Sample the eccentricity such that  $\frac{dN}{de} \propto e$ , i.e., a thermal distribution of eccentricities.
5. Compute the true anomaly by assuming a uniform distribution of time points along the orbit:  $t_{\text{orbit}} \in [0, P_{\text{orbit}}]$ . This corresponds to a uniform mean anomaly distribution.

With this recipe, we generate a cluster containing 100,000 stars and calculate the phase-space coordinates. We then discard the  $z$  coordinates and draw a new  $z$  coordinate from the  $z$ -prior distribution. From this cluster we choose  $N$  stars, as many as our data sample contains, taking into account the observational biases from the fields covered. This yields a mock data set that we analyze the same way as the real data in Section 3.1. This procedure is repeated 10,000 times, creating 10,000 mock data sets from which we calculate the mean and standard deviation in each pixel.

## Appendix B

### $z$ Priors Used in Previous Studies and Their Biases

In the following, we describe the  $z$  priors used in previous studies, the stellar cusp prior and the uniform acceleration prior. We show that both priors generate biased posterior distributions, in which the angular momentum distribution is not isotropically distributed on a sphere.

#### B.1. The Stellar Cusp Prior

Bartko et al. (2009) introduced the stellar cusp prior. The distribution of  $z$  coordinates is given by

$$P(z|x_{\text{obs}}, y_{\text{obs}}) \propto (x_{\text{obs}}^2 + y_{\text{obs}}^2 + z^2)^{-\frac{\beta+1}{2}}, \quad (\text{B1})$$

where  $\beta=2$  is the power-law index of the intrinsic density profile of the cusp in the GC  $dN/dR \propto R^{-\beta}$  (Genzel et al. 2003), and  $x_{\text{obs}}/y_{\text{obs}}$  stand for the observed star positions.

The simulated cluster analysis with the stellar cusp prior correctly captures the input distribution of eccentricities and also the distribution of semimajor axes is reproduced closely. However, the argument of pericenter  $\omega$  does not follow a uniform input distribution, and high inclinations are favored. This results in a boxy distribution of stars, with an overdensity toward the center (see Figure 13).

The reason for this behavior lies in the distribution of eccentricities. While the positions of the stars geometrically follow a power-law slope, the probability for  $z$  given  $R_{\text{obs}}$  depends on how much the individual star plunges toward the black hole. When one knows the distribution of eccentricities and the distribution of semimajor axes, this ‘‘plunging in’’ is given by the observed velocity vector  $\vec{v}$ , a piece of knowledge that is ignored in this prior.

#### B.2. The Uniform Acceleration Prior

The uniform acceleration prior has first been used by Lu et al. (2009) and is constructed by drawing the acceleration  $a_S(R)$  uniformly in the possible range, i.e.,  $a_S(R) \in \left[ GM_*/(z_{\text{max}}^2 + R^2)^{3/2}, \frac{GM_*}{R^2} \right]$ . The maximum value

for  $a_S(R)$  is reached for  $z=0$ , and its minimum value is obtained from the maximum allowed  $z_{\text{max}} = \sqrt{2GM_*/|\vec{v}|^2 - R^2}$ . The  $z$  coordinate is then obtained from

$$z = \sqrt{\left( \frac{GM_* R_{\text{obs}}}{a_S(R)} \right)^{2/3} - R^2}. \quad (\text{B2})$$

The analysis with the uniform acceleration prior does not reproduce the linear distribution of eccentricities and produces a tail of high semimajor axes orbits. Similar to the stellar cusp prior, the argument of periaapsis  $\omega$  is not uniformly sampled but shows an angular dependence. Furthermore, the orbital nodes are biased toward high values, but without the clear concentration toward  $\cos(\phi) = \pm 1$  of the stellar cusp prior. Inspecting the distribution of  $z$  values, one can make out a zone of avoidance close to zero. Nevertheless, at least perceptually, the uniform acceleration prior seems to fare slightly better as the distribution of  $z$  values is more symmetrical than that for the stellar cusp prior.

The reason for the mismatch from an isotropic cluster lies again in the eccentricity distribution  $\frac{dN}{d\epsilon} \propto \epsilon$ . Because most stars have eccentric orbits there is a high chance of observing a star far away from the black hole and close to apocenter, where the acceleration is low. Therefore, the distribution of acceleration is not uniform but varies radially and depends on the velocity  $\vec{v}$  of the star.

For both the stellar cusp and the uniform acceleration prior, the reason why the prior clusters deviate from that of an isotropic cluster is that the priors only depend on the projected radius  $R_{\text{projected}}$  and do not take the velocity of the star into account.

#### B.3. Comparison of the Different Priors

In this appendix, we compare the two different priors that have been used in the past with the isotropic cluster prior. Figure 12 compares the  $z$ -probability distribution functions for the three priors and the example star E29. For the stellar cusp prior and the isotropic cluster prior, the analytic expressions are

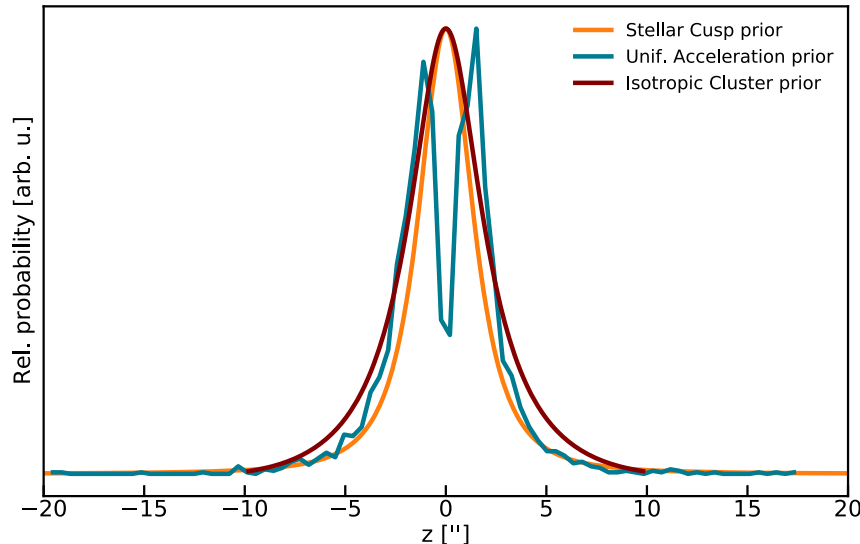


**Figure 12.** Comparison of the PDF of the  $z$  values for the star E29: The orange line shows the PDF of the stellar cusp prior (Equation (B1)), the blue line shows the histogram of  $z$  values sampled according to the uniform acceleration prior (Equation (B2)), and the dark red line shows the isotropic cluster prior (Equation (5)). For better comparison, we have normalized the mode of the respective distributions to 1.

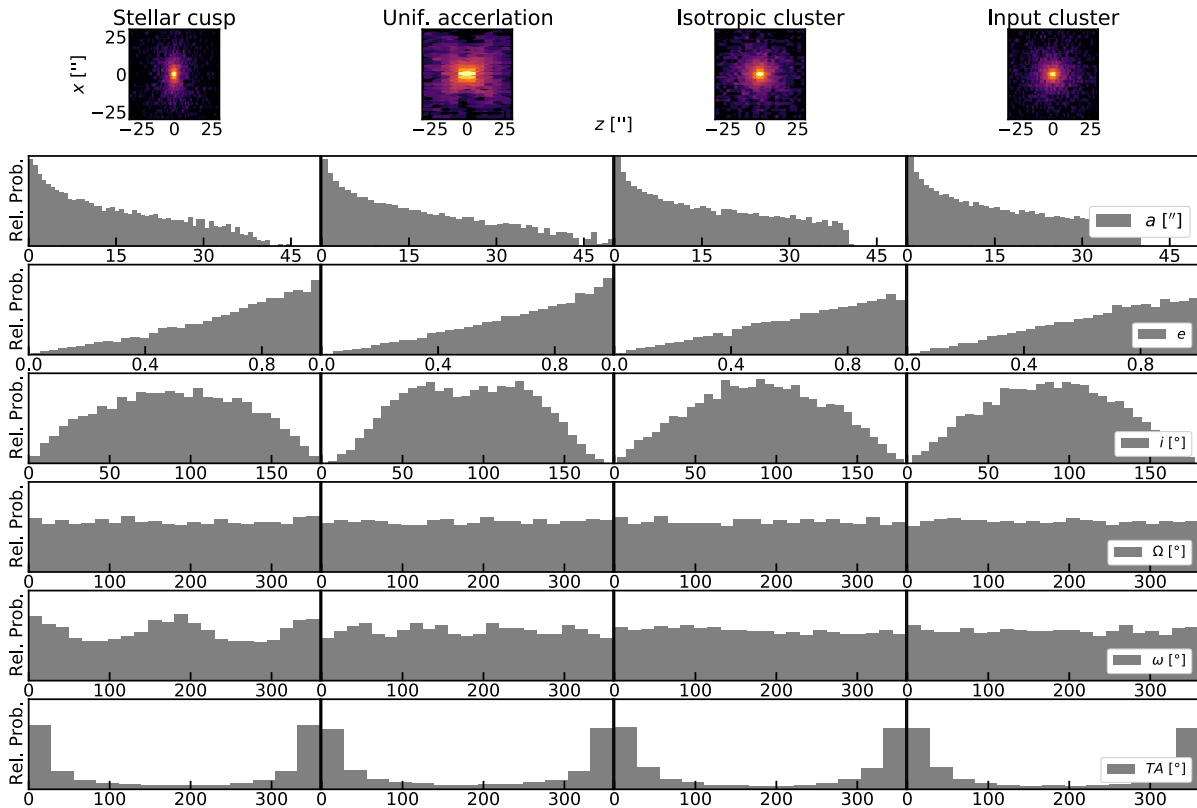


**Figure 13.** Distribution of orbital elements of different prior clusters, drawn from the stellar cusp prior, the uniform acceleration prior, the isotropic cluster prior, and the input isotropic cluster. The top panel shows the  $z$  vs.  $x$  distribution of the different prior clusters. See Appendix B.3 for details.

given in Equation (B1) and Equation (5). For the uniform acceleration prior we estimate the PDF by making a histogram of the  $z$  values derived from the prior (see Equation (B2)).

Because the  $z$  PDFs are different, they will lead to different  $z$  distributions. To illustrate the effect on our null hypothesis of an isotropic cluster, we conduct the following numerical experiment:

1. Draw 10,000 stars from an isotropic distribution according to the recipe detailed in Section 3.4.
2. Discard the  $z$  coordinate of each star.
3. Redraw a  $z$  coordinate for each star from its respective prior distribution function.

We call the resulting cluster the “prior cluster,” in which each star has a new  $z$  position. We plot the resulting  $z$  versus  $x$  position in the top row of Figure 13 for each of the three priors as well as the input isotropic cluster. Plotting the  $z$  versus  $y$  coordinate yields a qualitatively identical plot. It is evident that the isotropic cluster prior best reproduces the input cluster.

To better compare the respective prior clusters with the input orbital elements we recompute the orbital elements of each star using the newly determined  $z$  position. Figure 13 compares the histogram of the input orbital elements with those computed from the resampled stars.

The isotropic cluster prior best reproduces the input orbital element distribution, and specifically, it does not yield biased distributions of  $i$  and  $\Omega$ , which are the parameters we are interested in. This is in contrast to the stellar cusp prior and the uniform acceleration prior. This behavior of the priors was discovered in previous studies (Bartko et al. 2010; Yelda et al. 2014), and both studies tried to debias their study by

subtracting the mean bias from the density histogram. Our unbiased prior makes this debiasing step unnecessary. We conclude that the isotropic cluster prior correctly maps the input isotropic cluster on a self-similar realization of itself. We therefore achieve a meaningful null hypothesis: how different is the observed angular momentum distribution is from that of an isotropic cluster.

We note that the isotropic cluster is not the “best” prior to determine the angular momentum distribution of the young stars in the GC. Given that the presence of at least one star disk is undisputed, a “stellar disk prior” would be more suited to determine the presence of the disk. Such a prior would however change the null hypothesis to “How different is the observed star distribution to the assumed stellar disk?” and is therefore not suited to find new kinematic features. Once the determinant of the volume-filling factor is determined the construction of such a “disk prior” is trivial and follows the method in Section 3.3, with the suitable changes to Equation (3).

### Appendix C Discrepancy between the Works of Bartko et al. (2009) and Yelda et al. (2014)

Both Bartko et al. (2009) (abb. Bartko09) and Yelda et al. (2014) (abb. Yelda14) agree on the presence and orientation of the clockwise disk, but the significance of the warp is disputed. This is surprising: While Yelda14 presented an improvement in all relevant numbers (number of stars, number of constrained stars, number of determined orbits) compared to the Bartko09 sample, the improvement is gradual. For example, the total number of young stars in the sample increased by 18 (from 98

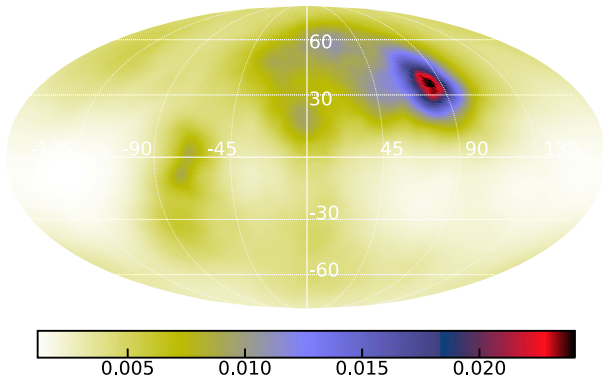


**Figure 14.** Comparison of the histogram of orbital nodes calculated in this work and presented in Figure 10 of Yelda et al. (2014). We have normalized the histogram to the same minimum and maximum values; see text for details.

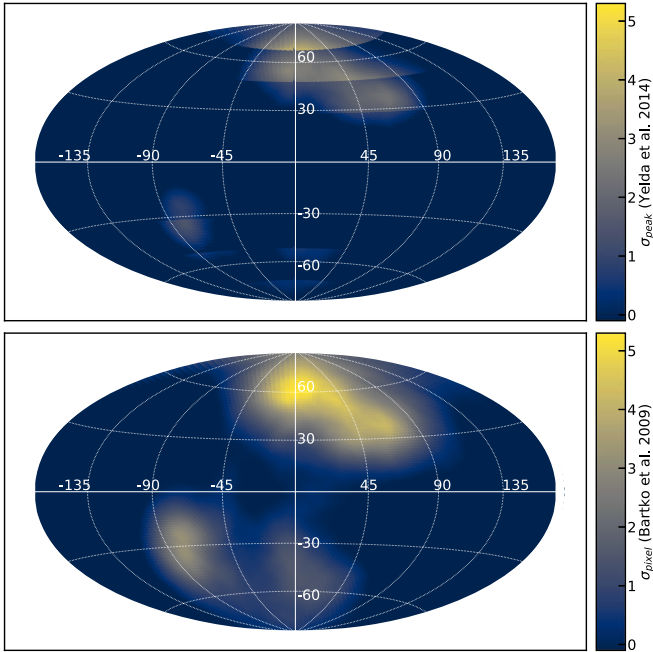


**Figure 15.** Difference between significance using the pixel and peak significance used in Bartko et al. (2009) and Yelda et al. (2014) for the radial slice ranging from  $3''2$  to  $6''5$ . The data used are taken from Yelda et al. (2014), and we use the uniform acceleration prior.

to 116), but the sample includes all 98 young stars from Bartko09.

In the following we try to explain the apparent discrepancy between the works. For this, we use the data set published in Yelda14 and use exclusively the uniform acceleration prior. We will show that the discrepancy between the work is not due to error but is dominated by the different definitions of the significance.

Figure 14 demonstrates that we can reasonably reproduce the Yelda14 results. The histogram has been normalized to match those of the bounds of the histogram of Yelda14 (Figure 10 in their work) and we use the same color map and projection.

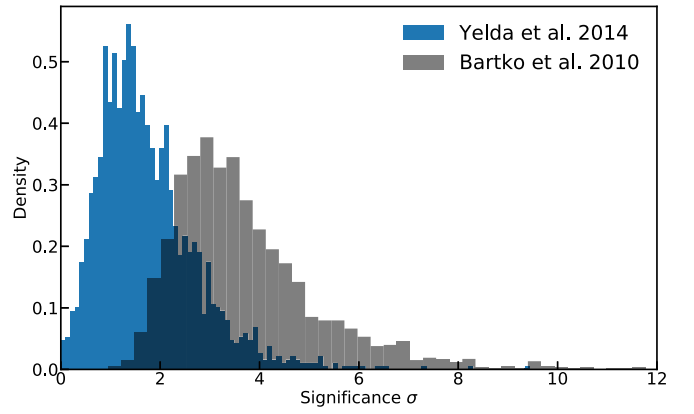


**Figure 16.** Histograms of the highest value of the significance calculated for each mock observation. The black histogram shows the pixel significances  $\sigma_{\text{pixel}}$  (Bartko et al. 2009), and the blue histogram shows the peak significance  $\sigma_{\text{peak}}$  (Yelda et al. 2014), respectively.

There is broad agreement between the figure presented in Yelda14 and our reproduction.<sup>14</sup>

Bartko14 compute the pixel significance in the same manner as us:

$$\sigma_{\text{pixel}} = \frac{s_{\text{pixel,obs}} - \langle s_{\text{pixel,sim}} \rangle}{\text{rms}(s_{\text{pixel,sim}})}, \quad (\text{C1})$$

where  $s_{\text{pixel,obs}}$  stands for the pixel value in the observed histogram and  $s_{\text{pixel,sim}}$  stands for the simulated pixels of the mock observations. This is based on the standard approach described in Li & Ma (1983). In contrast, Yelda14 use the peak significance instead of pixel significance:

$$\sigma_{\text{peak}} = \frac{s_{\text{peak,obs}} - \langle s_{\text{peak,sim}} \rangle}{\text{rms}(s_{\text{peak,sim}})}, \quad (\text{C2})$$

where  $s_{\text{peak,obs}}$  stands for the observed peak value of a feature, and  $s_{\text{peak,sim}}$  stands for the respective peak values in the simulations. In order to account for the biases introduced by the observations and the uniform acceleration prior, they calculate the peaks in bins of  $20^\circ$  in latitude. Figure 15 shows the difference in reported significance between the two methods for the radial slice ranging from  $3''2$  to  $6''5$ .  $\sigma_{\text{peak}}$  is much reduced compared to  $\sigma_{\text{pixel}}$ , and we recover the two seemingly competing conclusions found in Bartko09 and Yelda14: Using the pixel significance we find a significant feature at  $\sim 6\sigma_{\text{pixel}}$  (see Figure 11 of Bartko09). In contrast, using the peak significance is  $\sigma_{\text{peak}} \lesssim 3$ .

In the following, we explore the differences between the two definitions of the significance. Using a set of 2000 mock observations of an isotropic cluster resembling our observations, we calculate the feature with the highest significance for each of the mocks. The histogram of these significances is shown in Figure 16. The peak significance is more conservative, with the mode of the significance corresponding to  $\sim 2\sigma_{\text{peak}}$ , while significances of  $\sim 6\sigma_{\text{pixel}}$  are routinely observed

<sup>14</sup> However, minor discrepancies exist. For instance, the faint feature next to the clockwise disk is “fuzzier” in our reproduction. We speculate that this is most likely due to different treatment of unbound stars in the Monte Carlo simulations, which we do not resample. Further, the strength of the smoothing seems decreased compared to Yelda14.

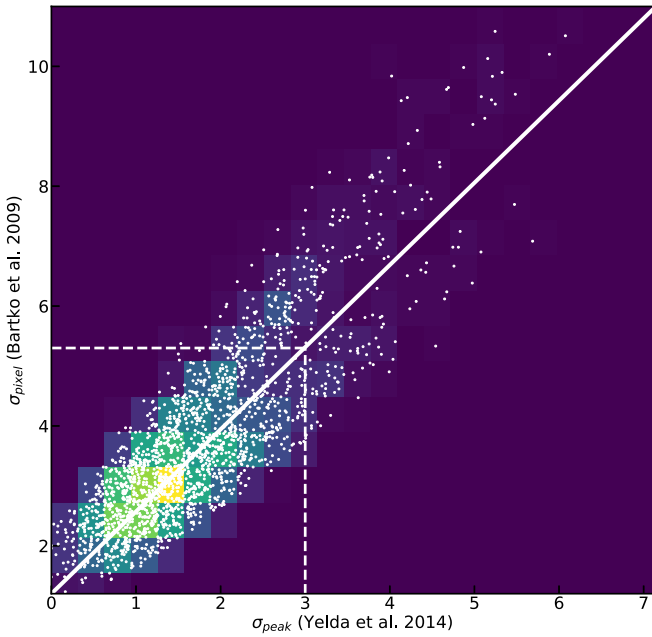


**Figure 17.** 2D histogram of the peak and the pixel significance calculated for 2000 mock observations. The white dots indicate the individual significance values, the thick white line indicates the trend. The horizontal dashed line indicates the peak value of  $\sigma_{\text{pixel}}$  found in Figure 15, and the vertical dashed line presents the projection again consistent with the respective  $\sigma_{\text{peak}}$  in Figure 15.

for the pixel significance. Despite this, the histograms are very similar and seem to be merely shifted realizations of each other.

This becomes even clearer when plotting the respective peak significance against the pixel significance of each mock observation (Figure 17). There exists a linear trend between the two definitions (indicated by the trend line). The horizontal dashed line indicates the maximum significance  $\sigma_{\text{pixel}}$  found in the upper panel of Figure 15 ( $\sim 5.3\sigma$ ), and the vertical line

**Table 3**  
Confidence Percentiles Corresponding to  $\sigma_{\text{pixel}}$ , Rounded to the Integer,  
Derived from 100,000 Mock Simulations

Confidence Percentile	Corresponding $\sigma_{\text{pixel}}$
68%	$\sim 4 \sigma_{\text{pixel}}$
95%	$\sim 7 \sigma_{\text{pixel}}$
99%	$\sim 10 \sigma_{\text{pixel}}$
99.9%	$\sim 18 \sigma_{\text{pixel}}$
99.99%	$\sim 31 \sigma_{\text{pixel}}$
99.999%	$\sim 42 \sigma_{\text{pixel}}$

shows the projection onto  $\sigma_{\text{peak}} = 3$ , which is consistent with the lower panel of Figure 15.

The differences between the two methods are interesting, and it is clear from Figure 17 that the significance  $\sigma_{\text{pixel}}$  is inconsistent with the confidence ranges associated with the Gaussian  $\sigma$ . This is not a new problem, and the difficulty of finding the confidence ranges of Monte Carlo simulations is commonly discussed in other astronomical observations (see for instance Section 4.4 in H.E.S.S. Collaboration et al. 2018 and Stewart 2009). In order to assess the significance in terms of confidence levels, we calculate the maximum pixel significance in 100,000 mock observations. Deriving the percentiles of this maximum pixel significance distribution thus allows us to estimate probability values up to ( $p \sim 99.999\%$ ), which we give in Table 3.

## Appendix D

### Combined Posterior Distributions of Kinematic Features

Figure 18 shows the combined posterior distribution for stars belonging to the respective kinematic features (i.e., with  $\Delta$  evidence  $< 2$ ).



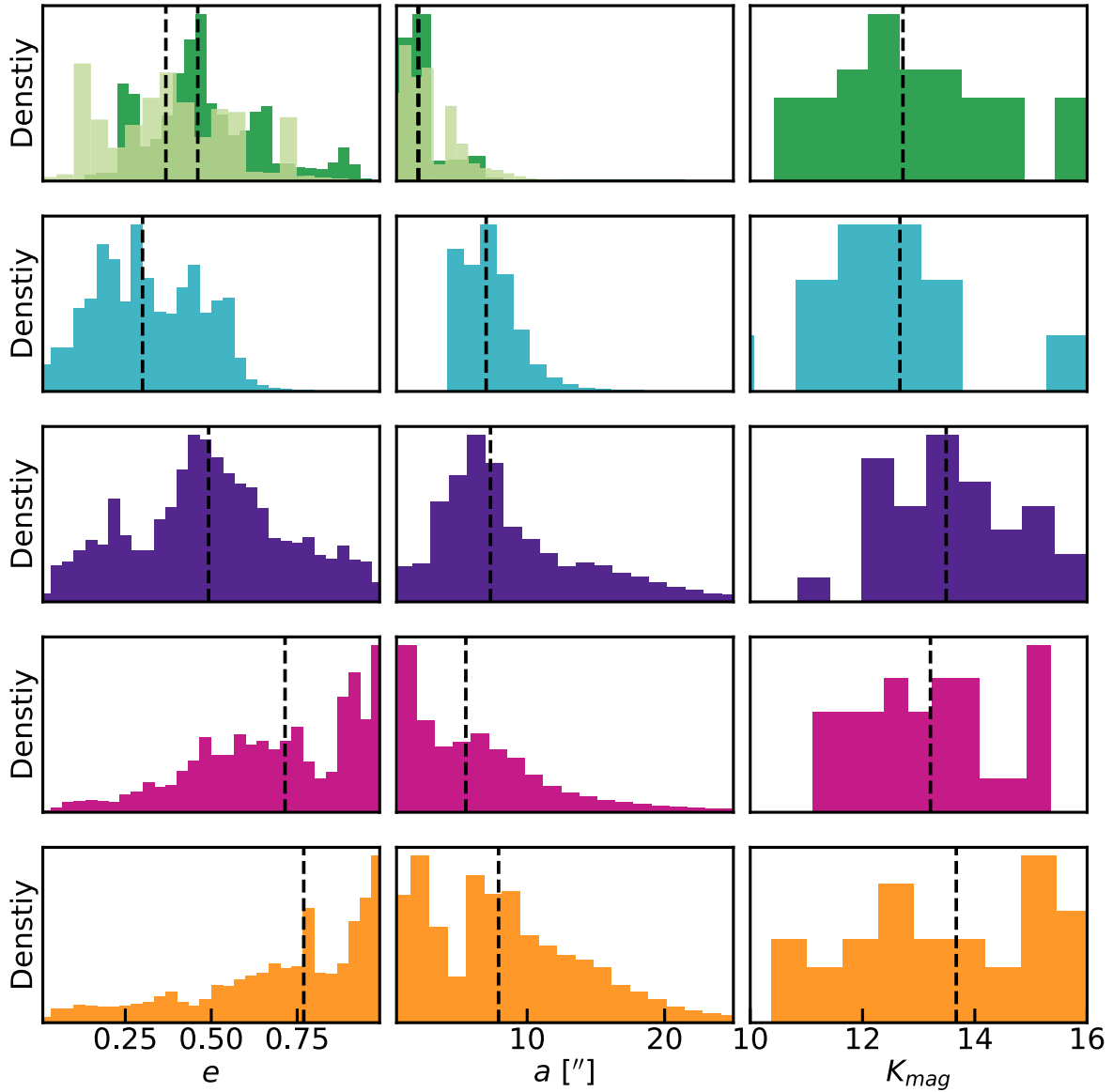


**Figure 18.** Comparison of the eccentricity distributions, the semimajor axis distributions, and  $K_{\text{mag}}$  distributions of the different kinematic features. The top row includes both the distributions of the 5D-constrained stars (dark green) and the stars with determined orbital solutions (light green) of CW1. CW2 is shown in light blue, CCW/F1 in purple, F2 in pink, and F3 in orange.

## Appendix E

### Uncertainty Estimation of the Completeness Correction

Because we do not treat the KLF as a probabilistic quantity, we need to propagate the uncertainty of the completeness correction to the KLF. To estimate the completeness uncertainty, we assume that the total number of stars in a given pointing is Poissonian and that the determined fraction is binomially distributed. Explicitly, for each pointing and magnitude bin, the Poisson rate parameter is  $\lambda = N_{\text{total}}$ , and the rate parameter of the binomial distribution is  $p = \frac{N_{\text{unclassified}}(m_K)}{N_{\text{total}}(m_K)}$ . This allows us to draw random samples of the completeness for each pointing and magnitude bin.<sup>15</sup>

---

```

n_samp=100
p=N_unclassified/N_total
completeness=np.empty(n_samp) #Pointing Complete.
n_total=np.empty(n_samp) #Pointing Total
Poisson=np.random.poisson
Binomial=np.random.binomial
for n in range(n_samp):
    n_total[n]=Poisson(N_total, n_samp)
    completeness[n]=Binomial(n_total[n], p)
completeness=1---completeness/n_total

```

---

Our estimate of the completeness is derived in patches, thus there is a perfect correlation of neighboring pixels within each patch. We account for this correlation by drawing random samples of patches rather than each pixel. With the thus-sampled completeness maps, we can compute the sampled effective area  $A_{\text{eff,sampled}}(R_1, R_2, m_K)$  for each realization. We

<sup>15</sup> Code snippet in Python.

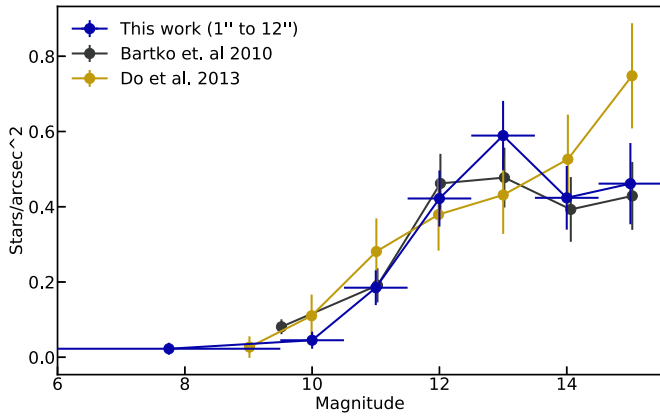


**Figure 19.** KLF of all young stars with projected radii ranging from  $1''$  to  $12''$  (black), compared to previously published KLFs by Bartko et al. (2010) and Do et al. (2013). In order to compare the KLFs, we have normalized the distributions so that the area under the respective curves up to  $K_{\text{mag}} = 13$  is 1.

determine the uncertainty of the effective area as the standard deviation of the sampled effective area and calculate the uncertainty of the KLF using Gaussian error propagation, which holds in the limit of many samples:

$$\sigma_{\text{KLF}} = \left( \left( \frac{\partial \text{KLF}}{\partial A_{\text{eff}}} \sigma_{A_{\text{eff}}} \right)^2 + \left( \frac{\partial \text{KLF}}{\partial N_{\text{stars,obs}}} \sigma_{N_{\text{stars,obs}}} \right)^2 \right)^{1/2}, \quad (\text{E1})$$

with  $\sigma_{N_{\text{stars,obs}}} = \sqrt{N_{\text{stars,obs}}}$ .

### Appendix F

#### Comparison of Different $K$ -band Luminosity Functions Reported in Previous Works

We compare the young-star KLF binned to projected radii from  $1''$  to  $12''$  derived here to ones published in Bartko et al. (2010) and Do et al. (2013) in Figure 19. To compare the three studies, we have normalized the curves with the area under the curve up to magnitude bin  $K_{\text{mag}} = 13$ , up to which the sample should be complete in all studies. The overall agreement between this work and Bartko et al. (2010) is good. While the star sample within  $12''$  is very comparable between this work and Bartko et al. (2009), the way the completeness is derived is fundamentally different. Furthermore, the number of bright stars in the brightest bin has decreased, which is due to refined magnitude measurements, which are typically lower than the ones reported in Bartko et al. (2010). The discrepancy of the KLF reported by Do et al. (2013) and Bartko et al. (2010) consequently remains.

### Appendix G

#### $K$ -band Luminosity Function of the Central Region

The scenario proposed by Chen & Amaro-Seoane (2014) connects the dynamically distinct S-star cluster to the young stars in the clockwise disk. There is no commonly accepted definition of S stars, and typically the term also refers to central old stars. Here we define as an S star those young stars within  $0''.8$ . Because the central region is populated by stars typically fainter than  $K_{\text{mag}} = 14$ , including these stars in the  $K$ -band luminosity function of the CW disk alters the KLF. Figure 20 displays the derived KLF and compares it to the other KLFs reported in Figure 11. If the S stars and CW disk indeed form a common structure, their KLF is less top heavy. We caution, however, that in such a scenario the KLF is not a direct tracer

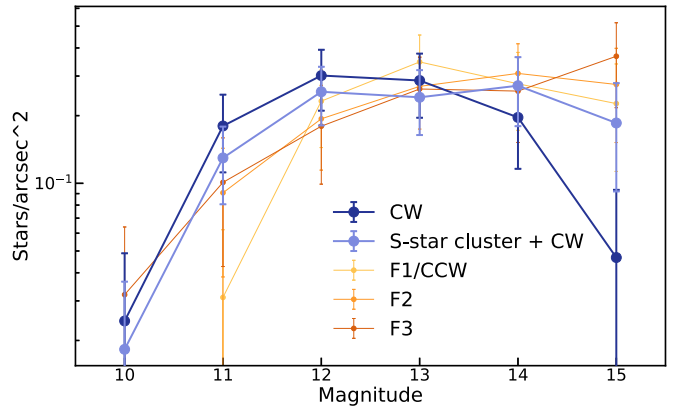


**Figure 20.** Similar to Figure 11, but including the combined KLF of the S star and the CW disk. As in Figure 11 and Figure 19, the KLFs have been normalized to make them comparable; see text for details.

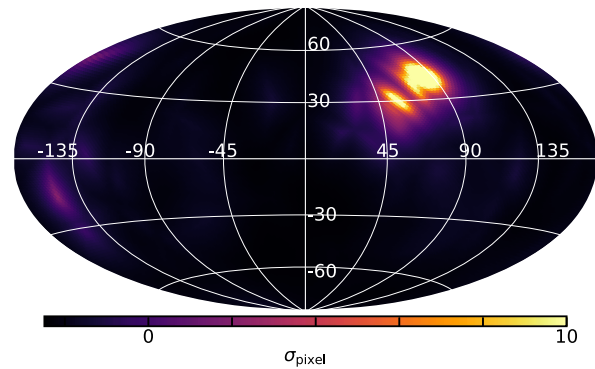


**Figure 21.** Like Figure 5 for the central arcsecond, plotted in linear scale. The color scale is truncated at  $10\sigma_{\text{pixel}}$ , which corresponds to a  $p$ -value of  $\sim 99\%$ .

of the initial mass function. In the Chen & Amaro-Seoane (2014) scenario, large stars are rapidly destroyed and thus do not appear in the star count. Further, this raises the question of including the other dynamical features and the other young stars not associated with any feature.

### Appendix H

#### Anisotropy in the Central Arcsecond

Ali et al. (2020) report an apparent overdensity in the inclination of the orbits of the early- and late-type stars in the central arcsecond. Figure 21 shows the significance of the overdensity of the angular momentum distribution of the young stars studied in this paper. No significant overdensity is discernible other than the inner onset of the clockwise disk being apparent. This result entails two caveats: Compared to Ali et al. (2020) we do not include late-type stars, and the significance is calculated based on the comparison against an isotropic cluster, which also entails constraints on all orbital elements.

### Appendix I

Table 4 gives the updated orbital elements of the young stars with orbits.

**Table 4**  
Stars with Determined Orbital Solutions

MPE	Pau.	UCLA	a (as)	$\sigma a$ (as)	$e$	$\sigma e$	$i$ ( $^\circ$ )	$\sigma i$ ( $^\circ$ )	$\Omega$ ( $^\circ$ )	$\sigma \Omega$ ( $^\circ$ )	$\omega$ ( $^\circ$ )	$\sigma \omega$ ( $^\circ$ )	$P$ (yr)	$\sigma P$ (yr)	$t_0$ (yr)	$\sigma t_0$ (yr)
S18			0.28	0.01	0.24	0.01	107.18	0.6	51.23	0.37	3.5	5.45	54.12	3.41	1989.75	0.74
S13	E3	S0-20	0.26	>0.01	0.43	>0.01	22.96	0.12	74.05	0.55	245.86	0.77	49.51	0.15	2004.89	0.01
S9	E9	S0-5	0.27	>0.01	0.64	>0.01	82.63	0.11	156.18	0.05	153.22	0.45	50.93	0.52	1977.35	0.4
S4	E6	S0-3	0.35	>0.01	0.4	>0.01	80.3	0.05	258.8	0.04	293.66	0.9	75.26	0.71	1959.39	0.73
S175			0.37	0.01	0.98	0.01	87.83	0.19	325.99	0.27	68.14	0.14	81.76	2.21	2009.51	>0.01
S14	E2		0.3	>0.01	0.99	>0.01	105.27	0.89	222.92	0.67	330.5	0.54	60.76	0.53	2000.32	0.03
S60			0.41	0.01	0.7	0.01	124.87	0.55	168.31	1.65	25.8	1.04	95.07	5.16	2024.8	0.27
S12	E5	S0-19	0.3	>0.01	0.89	>0.01	33.59	0.32	231.09	0.96	316.94	0.83	59.06	0.13	1995.58	0.03
S31	E7	S0-8	0.44	>0.01	0.56	>0.01	109.57	0.04	137.39	0.05	311.38	0.31	104.92	0.34	2018.16	0.01
S8	E10	S0-4	0.4	>0.01	0.81	>0.01	74.19	0.24	315.15	0.14	347.42	0.29	92.08	0.35	1983.95	0.19
S29			0.39	>0.01	0.97	>0.01	144.11	1.37	6.26	1.99	205.08	1.85	89.85	0.7	2021.43	0.02
S1	E4	S0-1	0.61	0.01	0.57	0.01	119.19	0.09	342.32	0.13	122.98	0.52	174.78	3.63	2001.79	0.07
S19			0.59	0.02	0.78	0.02	71.76	0.08	344.94	0.15	158.67	0.4	165.66	10.38	2005.64	0.03
S33			0.75	0.01	0.54	0.01	64.35	0.86	99.28	2.04	299.96	1.88	236.01	6.22	1904.31	8.04
S42			0.38	0.01	0.75	0.01	39.85	0.18	319.29	1.88	42.63	1.14	84.42	2.25	2022.59	0.08
S67	E15	S1-3	1.16	0.01	0.27	0.01	135.66	0.48	95.9	3.04	208.75	0.81	453.13	6.77	1685.57	10.92
S71			0.98	0.01	0.9	0.01	74.18	0.13	34.84	0.29	338.96	1.19	354.7	3.65	1686.51	3.86
S66	E17	S1-2	1.37	0.02	0.14	0.02	131.64	0.5	92.87	2.12	121.65	8.01	583.93	14.64	1774.34	21.17
S96	E20	S1-11	1.56	0.03	0.13	0.03	126.14	0.46	115.64	0.36	234.1	1.9	710.53	20.48	1623.76	8.99
S91			1.91	0.07	0.34	0.07	115.63	0.24	110.07	0.18	344.37	0.65	957.92	52.64	1075.96	52.77
S83	E16	S0-15	1.18	>0.01	0.17	>0.01	129.95	0.05	97.04	0.2	188.27	0.02	464.74	0.88	2022.31	0.49
R14	E22	S1-14	2.78	0.08	0.44	0.08	118.86	0.25	113.28	0.76	158.8	1.17	1659.39	73.8	3510.03	74.77
S97	E23	S1-16	2.41	0.38	0.37	0.38	113.6	1.03	112.67	0.99	24.61	9.26	1360.81	325.27	2125.26	19.9
R44		S2-21	4.97	0.48	0.39	0.48	127.85	1.11	85.3	1.72	218.21	3.1	3964.44	576.82	1934.91	13.95
S87	E21	S1-12	4.14	0.03	0.36	0.03	115.27	0.2	106.64	0.84	305.55	5.76	3059.27	29.16	-877.69	40.06
S2	E1		0.12	>0.01	0.88	>0.01	134.68	0.03	228.17	0.03	66.26	0.03	16.05	>0.01	2018.38	>0.01
R34			1.85	0.02	0.61	0.02	136.94	0.36	333	1.37	58.88	0.88	902.73	13.67	1506.63	9.97
S22			1.06	0.02	0.39	0.02	107.7	0.12	291.01	0.14	84.69	1.98	398.26	10.27	1991.82	0.85
S6	E11	S0-7	0.65	0.01	0.85	0.01	87.5	0.07	84.46	0.13	117.36	0.51	190.3	3.14	2111.16	1.85
R85	E56	I.34W	6.59	1.7	0.34	1.7	128.27	2.87	110.77	1.03	181.05	2.38	6055.99	2343.35	2019.38	31.46
R70	E54	S4-36	3.48	0.01	0.35	0.01	147.27	0.18	115.55	0.98	43.19	1.8	2326.65	12.68	3667.56	16.75
R1	E29	S2-7	2.63	0.06	0.53	0.06	125.09	0.32	117.28	1.52	243.87	1.17	1523.25	50.46	4005.64	45.51
S5	E8	S0-26	0.53	0.01	0.72	0.01	115.96	0.37	128.58	0.81	271.99	0.4	140.03	3.4	1954.49	1.41
S72	E18	S1-8	2.2	0.05	0.33	0.05	119.18	0.36	316.04	0.64	205.09	1.97	1184.02	41.41	1055.3	41.4
R39	E40	S3-5	3.22	1.46	0.01	1.46	122.23	8.07	107.05	0.05	359.99	4.71	2067.22	1403.78	2054.44	27.1
R30	E32	S2-15	6.36	0.14	0.61	0.14	113.02	0.38	94.51	1.49	12.33	1.74	5739.49	184.24	2242.8	7.55

Note. Pau. abbreviates Paumard et al. (2006).

## Appendix J

Table 5 gives the phase space coordinate measurements of the young stars without orbits.

Figure 22 indicates the young stars' projected location and the reference number given in Table 5.

**Table 5**  
Young Stars without Determined Orbital Solutions

#	Tri. ID	Pau. ID	UCLA ID	Alt. names	$K_{\text{mag}}$	$R$ (")	Sou. vLSR	R.A. (")	$\sigma$ R.A. (mas)	Decl. (")	$\sigma$ Decl. (mas)	$v_{\text{R.A.}}$ ( $\text{km s}^{-1}$ )	$\sigma v_{\text{R.A.}}$ ( $\text{km s}^{-1}$ )	$v_{\text{Decl.}}$ ( $\text{km s}^{-1}$ )	$\sigma v_{\text{Decl.}}$ ( $\text{km s}^{-1}$ )	$v_z$ ( $\text{km s}^{-1}$ )	$\sigma v_z$ ( $\text{km s}^{-1}$ )
0	41		S7-216	L6W	10.9	7.9	t.w.	-7.73607	0.13	1.39504	0.18	87.5	1.7	202.2	2.8	71.0	36.9
1	163	E35	S2-16	I.29 NE1	12.3	2.3	Pau.	-1.00111	0.09	2.06472	0.07	-349.2	0.6	-48.9	0.4	-98.1	68.5
2	283	E36	S2-19		12.7	2.3	Pau.	0.44190	0.08	2.29963	0.09	-319.9	0.4	26.0	0.5	41.2	18.8
3	571		S3-17		13.5	3.2	MPE	-1.41736	0.64	2.84290	0.33	256.3	9.3	60.6	4.9	-67.4	50.7
4	387	E38	S2-74	R46	13.2	2.8	Pau.	0.18116	0.09	2.76872	0.09	-341.6	0.5	36.6	0.4	35.2	22.8
5	349	E61		I.34NW	13.2	4.7	Pau.	-3.75269	0.14	2.83748	0.15	-213.2	2.3	-159.9	1.8	-151.4	29.8
6	149		S6-89		12.0	6.2	Pau.	5.44076	0.13	3.02582	0.13	98.1	1.9	-246.2	1.9	-128.5	67.2
7	238				12.5	11.4	t.w.	10.88630	0.17	3.25710	0.12	-64.8	2.3	-110.7	1.7	-130.7	28.1
8	640	E44	S3-25	R81	13.8	3.3	MPE	1.46037	0.13	2.94958	0.12	-278.8	0.6	9.8	0.7	-85.7	27.3
9	276	E59	I.7SE	I.7SE R60	13.1	4.6	Pau.	2.95516	0.14	3.46359	0.12	225.8	0.9	-0.6	0.7	-151.9	96.6
10	256		S7-236		12.7	7.9	t.w.	-7.08677	0.12	3.59196	0.12	-92.7	1.9	-174.1	1.5	-90.6	73.9
11	496	E52	S3-331		13.6	3.8	t.w.	-1.24685	0.13	3.63401	0.12	227.5	1.5	158.0	1.7	-154.3	42.7
12	566				13.7	8.9	t.w.	-7.82635	0.27	4.20889	0.28	14.8	6.3	167.7	6.1	-135.0	53.8
13	289	E85	S10-7		12.6	10.7	t.w.	9.71444	0.08	4.42600	0.13	-21.6	1.2	-158.5	2.0	-147.6	40.3
14	412		S5-235		13.2	5.3	t.w.	2.78624	0.12	4.55223	0.15	-41.0	1.6	-154.8	2.0	-66.5	51.3
15	124	E62	S4-364	R67	12.1	5.0	t.w.	2.19868	0.11	4.48614	0.10	243.7	0.7	-103.4	0.6	-150.9	36.5
16	327	E70	S6-93	I.7E1 (ESE)	12.7	6.7	Pau.	4.44120	0.15	4.96573	0.13	183.8	6.0	-46.6	5.2	-82.2	86.4
17	228	E66	S6-90	I.7SW	12.4	6.3	Pau.	-3.95089	0.14	4.92088	0.17	6.5	2.1	-138.3	2.5	-348.9	53.5
18	194				12.1	8.7	t.w.	6.94696	0.21	5.20279	0.14	124.7	2.3	-112.6	2.1	-216.6	44.3
19	72		I.10W	I.10W	11.0	8.3	t.w.	6.50133	0.55	5.14416	0.49	-39.5	17.7	191.3	20.6	-164.4	53.6
20	141				11.9	5.9	Pau.	0.89591	0.13	5.80990	0.12	-97.8	1.9	125.5	1.8	-498.2	20.9
21	426	E68	S6-95	I.7W	13.3	6.5	Pau.	-2.42612	0.14	5.99296	0.13	187.5	4.6	5.6	3.6	-300.4	113.4
22	982				14.5	7.6	t.w. MPE	-4.71018	0.12	5.98147	0.16	66.0	1.7	168.9	2.4	-74.1	74.2
23	1075				14.8	7.0	t.w.	-3.12104	0.20	6.22993	0.22	-12.9	3.8	-146.7	4.2	-230.6	44.0
24	6039	E71	S6-100		13.8	6.7	Pau.	1.57264	0.33	6.50982	0.55	-193.6	6.7	105.6	11.0	-282.5	153.7
25	438		S7-19		13.3	7.5	t.w. MPE	-3.79957	0.14	6.49040	0.13	198.3	2.1	110.3	1.7	-51.8	52.8
26	145	E90			11.6	12.8	Pau.	10.89210	0.12	6.66659	0.22	7.2	1.7	-1.2	2.9	-192.0	39.0
27	667				13.7	9.8	t.w.	7.03130	0.18	6.81468	0.23	-112.3	4.4	-82.9	5.2	-199.7	78.3
28	563				13.7	7.1	t.w.	1.23737	0.21	6.95135	0.19	-86.4	2.7	-141.5	3.4	-131.2	43.7
29	462		S7-20		13.4	7.9	t.w. MPE	-3.70753	0.11	6.93792	0.12	193.1	1.5	90.3	1.5	-18.9	54.0
30	117	E73	S7-10		11.6	7.7	t.w.	-1.09174	0.09	7.63062	0.08	-176.7	1.3	-93.2	1.3	-143.5	30.8
31	450		S8-15		13.2	8.2	Yel.	-1.59329	0.12	8.03911	0.09	-114.9	3.9	-122.8	3.7	-9.2	49.7
32	6293				13.3	12.2	t.w.	9.17849	0.83	8.07686	0.80	84.6	52.9	19.4	18.7	-148.9	48.9
33	1050				14.4	14.1	t.w.	11.34287	0.19	8.44936	0.25	42.8	2.3	-57.1	3.2	-50.9	92.2
34	69	E75	S8-4		11.1	8.5	t.w.	-0.01747	0.10	8.54243	0.07	-30.8	5.5	132.1	6.5	-209.0	54.4
35	425		S9-13		13.2	9.3	t.w.	-3.02305	0.15	8.80299	0.12	103.7	1.9	113.8	1.8	-97.9	78.3
36	628	E77	S9-23		13.6	9.2	t.w.	-1.27069	0.15	9.14331	0.17	-94.3	2.1	-108.4	2.1	-218.9	103.3
37	892				14.1	13.3	t.w.	9.47072	0.29	9.27860	0.32	103.6	4.1	30.0	4.5	-133.1	41.8
38	6053				13.8	14.4	t.w.	10.94691	0.10	9.41759	0.22	92.2	17.8	0.2	0.3	-206.0	60.6
39	1077				14.7	11.9	t.w.	-7.00140	0.22	9.66195	0.15	11.9	4.4	-198.5	3.6	242.8	69.8
40	191	E83	S10-5	I.15SW	12.0	10.2	Pau.	-1.57109	0.14	10.03093	0.12	-53.1	2.4	-74.4	1.5	-171.9	63.4
41	110	E84	S10-4		11.3	10.2	t.w.	0.08287	0.11	10.24086	0.09	-79.7	1.7	31.9	1.3	-278.3	38.9
42	6049				13.8	12.1	t.w.	5.80365	0.73	10.59286	0.56	55.3	13.5	137.6	11.0	59.9	28.0
43	599				13.0	16.8	t.w.	12.89808	0.68	10.69651	0.20	-9.9	13.1	27.2	4.2	-356.0	103.4
44	6038	E86	S10-48		15.1	10.7	Pau. Yel.	-0.54099	0.25	10.72329	0.10	55.0	5.7	18.9	2.3	-208.1	49.6
45	6042				14.7	20.9	MPE	17.54567	0.43	11.36067	0.25	-75.6	8.9	-82.3	5.2	-20.3	51.6

**Table 5**  
(Continued)

#	Tri. ID	Pau. ID	UCLA ID	Alt. names	$K_{\text{mag}}$	$R$ (")	Sou. vLSR	R.A. (")	$\sigma$ R.A. (mas)	Decl. (")	$\sigma$ Decl. (mas)	$v_{\text{R.A.}}$ ( $\text{km s}^{-1}$ )	$\sigma v_{\text{R.A.}}$ ( $\text{km s}^{-1}$ )	$v_{\text{Decl.}}$ ( $\text{km s}^{-1}$ )	$\sigma v_{\text{Decl.}}$ ( $\text{km s}^{-1}$ )	$v_z$ ( $\text{km s}^{-1}$ )	$\sigma v_z$ ( $\text{km s}^{-1}$ )
46	153	E88	S11-5	I15NE	11.7	11.8	Pau.	1.36917	0.12	11.67842	0.13	-26.7	1.8	73.3	2.0	-63.1	40.0
47	6055	E89			14.4	12.3	t.w.	-0.00571	0.16	12.27541	0.52	94.7	3.7	21.2	8.9	-87.2	71.1
							MPE										
48	392				12.8	20.4	t.w.	15.79520	0.32	12.87517	0.37	68.7	6.0	100.7	6.9	10.4	44.3
49	797				13.9	19.4	t.w.	13.09939	0.27	14.29659	0.31	14.5	4.0	37.6	3.8	-61.4	58.0
							MPE										
50	2158				15.4	17.3	t.w.	7.89660	0.40	15.37209	0.49	-97.3	8.5	-66.3	9.7	-208.8	90.3
51	1029				14.4	16.7	t.w.	4.44112	0.25	16.12724	0.25	-49.0	5.1	-56.4	5.2	-136.4	45.3
52	10007			out.-1	12.0	28.8	Yel.	21.61571	131.45	19.01698	116.22	69.4	5.4	37.5	4.7	-55.0	47.0
53	6059			out.-2	14.9	22.4	Yel.	-6.04643	3.93	21.59581	3.77	87.9	10.4	85.7	11.3	0.6	55.1
54	6045	E48		I13E4	11.8	3.5	Pau.	-3.21112	0.09	-1.40829	0.29	-231.3	1.7	23.7	5.0	63.6	75.5
55	2794				15.4	14.4	t.w.	10.69713	0.26	9.58150	0.36	-36.0	3.7	36.4	4.8	-206.3	37.0
56	4002				15.8	24.8	t.w.	16.44464	0.70	18.58738	1.10	11.1	10.0	-97.2	14.8	-99.3	148.4
57	1519				15.1	10.1	t.w.	7.77190	0.28	6.41182	0.21	40.0	5.2	126.9	3.8	-200.2	61.7
58	999				14.7	8.4	t.w.	4.34736	0.81	-7.23252	0.25	-33.4	26.3	-150.4	7.7	209.4	105.2
							MPE										
59	1928				15.4	11.2	t.w.	-0.14564	0.16	-11.24421	0.43	-43.2	2.3	100.7	6.1	121.2	53.9
							MPE										
60	3221				15.9	11.2	t.w.	4.73808	0.27	10.11947	0.15	94.3	3.9	133.3	2.2	-34.2	61.0
61	505	E87	S11-21		13.5	11.2	t.w.	2.56980	0.14	10.94189	0.15	-81.9	2.0	-103.5	2.2	-199.4	48.7
62	1984				15.4	9.3	t.w.	-5.60366	0.22	-7.38477	0.20	114.0	3.1	77.6	2.5	181.6	66.9
63	5027				16.7	21.2	t.w.	17.34700	0.51	12.11384	0.60	67.6	6.7	66.3	8.7	-58.3	45.0
64	3636				15.8	20.7	t.w.	17.56689	0.87	10.85727	0.86	52.9	30.0	30.6	36.8	-58.0	41.3
65	1697				15.4	8.7	t.w.	-4.79071	0.39	-7.23401	0.41	83.9	9.4	-166.9	9.3	146.7	103.1
66	2054				15.4	5.6	t.w.	-5.63960	0.42	-0.07162	0.41	124.8	10.0	97.6	9.2	40.0	92.5
67	172		S7-228		12.0	7.9	t.w.	-7.74674	0.12	1.68575	0.19	102.6	1.6	87.6	2.5	159.1	53.6
							MPE										
68	924				14.3	15.2	t.w.	-10.83416	0.35	-10.59268	0.22	21.6	10.2	-25.1	6.0	150.8	31.5
69	4273				16.6	11.6	t.w.	4.88054	0.48	10.53533	0.43	85.2	12.0	72.6	10.2	-207.1	147.0
70	32	E46		I13E1	10.7	3.4	t.w.	-2.95920	0.28	-1.64916	0.14	-139.4	3.5	-107.1	1.7	34.9	29.6
71	164	E28	S2-4	I.16 SSE2	12.3	2.1	Yel.	1.47277	0.06	-1.47447	0.06	313.8	0.4	103.0	0.4	208.2	27.8
72	10005		S2-50		15.3	2.3	Yel.	1.70018	0.16	-1.50870	0.13	78.1	2.2	66.0	1.4	-52.1	112.3
73	1307		S3-3		15.1	3.1	Yel.	3.08004	0.22	-0.65759	0.33	134.5	3.7	152.6	5.3	45.4	29.4
74	385		S1-1	R6	13.5	1.0	Gil.	1.04560	6.27	0.03311	5.97	227.1	0.2	44.6	0.4	536.0	0.0
75	6082			S93	15.4	1.1	Gil.	1.07884	0.12	0.16520	0.16	-114.7	1.5	-94.6	2.2	159.1	28.7
76	1342	E13	S0-31		15.4	0.7	Gil.	0.56887	10.21	0.44755	11.12	247.2	0.6	34.4	0.5	-262.7	100.1
77	1333	E12	S0-11		15.6	0.5	Gil.	0.49518	11.49	-0.06380	13.57	-140.5	0.4	-110.2	0.4	-41.6	67.0
78	832		S0-9		14.7	0.6	Gil.	0.22690	14.66	-0.60635	12.81	345.3	0.3	-210.7	0.3	156.7	54.1
79	6077				17.9	0.4	Gil.	0.19781	32.36	0.29388	32.32	299.1	9.8	-321.6	19.0	270.5	68.7
80	6084		S1-33		15.1	1.2	Yel.	-1.23863	0.10	-0.03386	0.09	-11.2	0.6	192.7	0.5	3.2	16.6
81	10006		S2-58		14.0	2.5	Yel.	2.15342	1.66	-1.17055	2.62	-28.1	0.8	255.1	1.2	61.9	31.3
82	6296		S3-314		15.5	3.8	Yel.	3.83020	1.79	-0.12036	2.31	118.9	1.2	160.2	1.3	13.3	18.2
83	178		S3-2		12.2	3.1	Yel.	3.06459	0.10	0.54448	0.10	160.6	0.7	30.4	0.8	-447.2	22.9
84	388		S5-237		13.2	5.6	Yel.	5.50480	0.19	0.98012	0.33	-59.4	3.3	244.6	4.7	34.5	16.1
85	469	E57	S4-169		13.5	4.4	Pau.	4.42516	0.12	0.25988	0.11	-106.7	1.8	150.6	1.8	-84.2	50.6
							t.w.										
86	519	E72	S6-82		13.6	6.7	Pau.	6.71581	0.21	-0.48061	0.34	60.2	3.5	209.3	5.9	91.0	102.7
87	4862				16.7	14.5	t.w.	9.96849	0.28	10.50405	0.45	43.8	9.4	64.3	10.6	-52.2	152.4
							MPE										
88	1282		S2-76		15.2	2.8	Yel.	-0.23156	0.24	2.80308	0.23	14.2	3.4	41.7	2.6	-18.9	69.6
89	229				12.7	11.4	t.w.	1.58128	0.10	-11.28210	0.16	-41.2	1.6	-18.0	2.4	162.4	67.4

**Table 5**  
(Continued)

#	Tri. ID	Pau. ID	UCLA ID	Alt. names	$K_{\text{mag}}$	$R$ (")	Sou. vLSR	R.A. (")	$\sigma$ R.A. (mas)	Decl. (")	$\sigma$ Decl. (mas)	$v_{\text{R.A.}}$ ( $\text{km s}^{-1}$ )	$\sigma v_{\text{R.A.}}$ ( $\text{km s}^{-1}$ )	$v_{\text{Decl.}}$ ( $\text{km s}^{-1}$ )	$\sigma v_{\text{Decl.}}$ ( $\text{km s}^{-1}$ )	$v_z$ ( $\text{km s}^{-1}$ )	$\sigma v_z$ ( $\text{km s}^{-1}$ )
90	497				13.7	10.2	t.w.	0.99022	0.11	-10.13985	0.14	-91.1	1.8	-115.5	2.0	55.1	70.9
91	634				13.9	14.5	t.w.	-10.63798	0.32	-9.84287	0.21	-62.2	12.7	89.3	5.6	100.0	38.8
92	78				11.4	9.4	t.w.	0.75508	0.11	-9.33208	0.11	58.6	1.4	61.3	1.4	195.7	50.1
93	96	E80	S9-9	I.9SE	11.8	9.9	Pau.	5.65695	0.15	-8.18150	0.19	-52.1	2.0	-67.0	2.6	119.5	106.1
94	6040	E76	S9-20	I.9SW	13.2	9.1	Pau.	4.30397	0.32	-8.03425	0.38	84.7	6.8	42.5	9.9	191.1	66.5
95	157		S8-7		12.1	8.3	t.w.	-3.69044	0.18	-7.42071	0.17	186.3	3.6	-21.2	2.7	60.0	30.2
96	243		S7-16		12.7	7.4	t.w.	1.62069	0.11	-7.24675	0.12	75.5	1.8	143.6	2.3	135.4	74.7
97	6295				12.1	8.8	t.w.	5.25694	0.34	-7.07123	0.30	8.0	6.7	36.7	6.3	207.0	107.2
98	63	E79	S9-114	AF	11.0	9.5	t.w.	-6.50895	0.17	-6.90214	0.27	101.0	2.8	60.8	4.6	155.7	50.2
99	71	E69	S6-63		11.4	6.6	t.w.	1.84516	0.13	-6.31453	0.11	227.7	2.1	60.0	3.4	140.8	39.7
100	210				12.3	8.0	t.w.	5.40038	0.20	-5.95261	0.19	-137.6	3.1	-104.7	2.6	-16.6	52.0
101	619				13.6	16.7	t.w.	15.63094	0.28	-5.86463	0.23	254.2	8.3	151.8	5.6	-83.3	88.9
102	73				11.2	10.6	t.w.	-8.92005	0.15	-5.74358	0.14	107.2	2.0	59.6	2.1	111.9	18.8
103	169	E65	I.9W	I.9W	12.1	6.3	Pau.	2.87892	0.12	-5.60405	0.15	204.2	1.9	136.5	2.1	136.9	67.1
104	423		S5-187	S5-187	13.2	5.8	t.w.	-1.70504	0.14	-3.53100	0.16	-33.5	1.9	-155.9	2.4	10.4	52.8
105	371				13.0	6.8	t.w.	-3.93026	0.73	-5.54228	0.44	234.8	9.6	-155.5	7.4	38.7	47.6
106	183				12.2	7.4	t.w.	4.85346	0.17	-5.54619	0.14	86.6	1.9	208.5	1.9	19.4	55.8
							MPE										
107	364				13.1	7.8	t.w.	-5.51646	0.20	-5.56841	0.20	-18.4	4.1	196.4	4.3	57.5	46.4
108	6041	E82	S10-136		13.2	10.1	Pau.	-8.61883	0.24	-5.31270	0.40	-80.1	4.6	139.5	9.3	-72.1	72.7
109	310		S5-191		12.9	5.8	t.w.	3.18965	0.19	-4.86952	0.16	-55.2	2.4	-141.3	1.9	107.0	38.5
110	218	E55	S4-71	R75	12.6	4.1	t.w.	0.77398	0.06	-4.06227	0.07	3.4	0.4	-174.5	0.4	63.6	50.8
111	914		S4-196		14.4	4.5	t.w.	2.22522	0.30	-3.93992	0.29	199.3	4.3	150.6	4.4	-27.8	115.0
112	136	E74	S8-181	AF NW	11.9	8.4	Pau.	-7.61325	0.12	-3.58604	0.15	-67.6	5.7	-141.5	3.1	54.6	73.5
113	112		S5-183	S5-183	11.6	5.8	t.w.	4.61476	0.13	-3.43525	0.15	-179.5	1.6	-78.0	2.0	-187.0	39.1
114	247				12.4	9.5	t.w.	-8.87355	0.11	-3.44397	0.14	-121.9	1.5	-74.3	2.6	67.6	52.6
							MPE										
115	313		S9-143		12.8	9.0	t.w.	-8.36240	0.12	-3.35608	0.13	24.5	1.7	-121.3	2.0	190.8	96.9
116	-1		S10-50		14.7	10.1	Yel.	9.54824	408.36	-3.18128	307.07	-19.0	7.8	-149.5	6.4	88.5	87.4
117	18	E41	I.33E	I.33E, R54	11.0	3.2	Pau.	0.66176	0.06	-3.12562	0.07	261.5	0.4	-55.0	0.4	169.7	20.5
118	383				13.2	11.2	MPE	-10.71378	0.11	-3.09565	0.15	-9.4	1.8	133.7	2.3	169.9	47.6
119	237	E47	S3-30	R42	12.6	3.4	t.w.	1.67000	0.07	-2.96310	0.05	-31.3	0.5	151.8	0.3	31.9	54.9
120	221	E53	S3-374	R64	12.7	3.9	Pau.	-2.74767	0.11	-2.82012	0.10	-19.4	0.6	-171.5	0.6	17.8	22.2
121	265		S8-196		12.6	8.6	t.w.	-8.08601	0.13	-2.90700	0.10	30.6	3.3	-64.7	3.7	208.9	49.6
122	6051	E43	S3-19		12.0	3.2	Pau.	-1.58166	0.15	-2.78548	0.09	287.5	4.6	-66.9	3.0	-122.5	47.2
123	6627		S7-30	S7-30	14.0	7.0	t.w.	6.47995	2.09	-2.67962	2.46	-101.1	7.3	-127.6	5.4	-27.4	48.9
124	578		S5-34		13.7	5.1	t.w.	-4.31319	0.35	-2.71983	0.82	-135.7	7.4	-125.1	16.2	18.6	78.7
125	320	E81	S9-283	AFN WNW	12.8	9.9	Pau.	-9.60670	0.20	-2.55478	0.15	64.6	2.6	-50.4	2.4	37.6	72.1
126	6044				15.0	6.4	t.w.	-5.83611	0.24	-2.53867	0.22	-131.2	7.2	51.3	7.0	239.3	21.0
127	64	E33	S2-13	I.33N	11.7	2.2	t.w.	-0.04844	0.06	-2.19802	0.09	135.8	0.4	-236.0	0.6	39.0	45.1
128	231	E45	S3-26		12.7	3.3	Yel.	-2.60948	0.08	-2.08260	0.08	224.4	0.5	52.4	0.5	60.1	30.3
129	10006		S4-262		16.8	4.7	Yel.	4.29051	26.47	-1.91401	22.00	-48.3	1.2	-196.0	2.1	39.9	57.9
130	30	E34	S2-17		11.2	2.3	t.w.	1.28217	0.06	-1.87551	0.06	354.3	0.3	-14.7	0.4	64.5	43.5
							MPE										
131	353		S6-96	S6-96	13.0	6.4	t.w.	-6.04464	0.25	-1.95065	0.39	-24.9	3.5	283.3	4.9	-20.1	51.9
							MPE										
132	956		S10-32	S10-32	14.5	10.3	t.w.	10.19469	0.15	-1.71080	0.14	110.9	1.7	150.5	2.3	214.8	73.6
133	94	E26	S1-24	I.16SSW	11.8	1.8	t.w.	0.72112	0.08	-1.60515	0.07	97.9	0.4	-258.3	0.4	153.5	40.3
134	34	E51	I.13E2	I.13E2	10.8	3.6	Fritz	-3.17210	0.14	-1.73202	0.25	-247.8	2.2	20.6	4.2	63.0	30.9
135	6046	E58	S7-180	I.3E	13.5	7.5	t.w.	-7.34555	0.22	-1.65065	0.27	-121.5	2.9	-32.9	3.5	103.5	38.3

**Table 5**  
(Continued)

#	Tri. ID	Pau. ID	UCLA ID	Alt. names	$K_{\text{mag}}$	$R$ ( $''$ )	Sou. vLSR	R.A. ( $''$ )	$\sigma$ R.A. (mas)	Decl. ( $''$ )	$\sigma$ Decl. (mas)	$v_{\text{R.A.}}$ ( $\text{km s}^{-1}$ )	$\sigma v_{\text{R.A.}}$ ( $\text{km s}^{-1}$ )	$v_{\text{Decl.}}$ ( $\text{km s}^{-1}$ )	$\sigma v_{\text{Decl.}}$ ( $\text{km s}^{-1}$ )	$v_z$ ( $\text{km s}^{-1}$ )	$\sigma v_z$ ( $\text{km s}^{-1}$ )
136	362	E60	S4-258		12.4	4.7	Pau.	-4.37896	0.14	-1.63966	0.13	-168.8	2.0	61.4	2.0	320.4	77.7
137	132	E30	S2-6	I.16SSE1 R29	12.3	2.1	Pau. Yel.	1.60887	0.05	-1.34653	0.06	306.2	0.4	72.5	0.4	179.9	25.5
138	386		S5-236	S5-236	13.3	5.7	t.w.	-5.55408	0.15	-1.29457	0.10	195.9	2.4	47.7	1.8	142.8	52.0
139	174	E50	S3-10	I.16SE3 R79	12.3	3.5	Pau.	3.34664	0.16	-1.13914	0.08	-22.1	1.0	198.4	0.5	306.0	60.3
140	928	E42	S3-96		14.3	3.2	Yel.	-3.13110	0.38	-0.66042	0.40	-33.9	5.7	207.4	6.1	41.8	45.1
141	266	E25	S1-22	W14	12.9	1.7	t.w.	-1.62041	0.07	-0.49944	0.04	310.8	0.4	-133.4	0.3	-293.6	95.9
142	562	E14	S0-14	R13 W9	14.0	0.8	Gil.	-0.75405	10.06	-0.28714	8.63	94.2	0.2	-58.9	0.2	-57.0	22.4
143	324		S2-22	R34	13.0	2.3	t.w.	2.31737	0.07	-0.24924	0.07	-66.3	0.9	232.8	1.0	91.4	43.6
144	1210				14.5	4.0	t.w. MPE	-3.97965	0.21	-0.07189	0.30	29.8	3.3	-8.0	4.1	-71.6	68.6
145	186	E64	S5-231		12.0	5.8	t.w. MPE	5.81326	0.35	0.08010	0.30	3.0	4.8	197.6	4.3	28.3	81.0
146	644		S7-161	S7-161	13.7	7.4	t.w.	-7.36747	0.12	0.05917	0.16	-72.3	2.2	-147.2	2.8	-31.6	76.2
147	396	E24	S1-21	W7	13.5	1.6	Yel.	-1.64325	0.05	0.10190	0.06	161.1	0.6	-219.9	0.9	-25.9	69.5
148	6080				15.7	1.1	MPE	-1.03195	0.69	0.21609	0.53	5.0	5.9	-183.9	4.9	-343.3	108.4
149	287	E78	S9-1	PMM20 01B1b	12.8	9.5	Pau.	9.45792	0.10	0.27966	0.12	-98.2	1.5	-108.5	1.6	-214.6	113.8
150	58	E67	S6-81	I.1E	11.1	6.4	t.w.	6.36728	0.21	0.25059	0.18	-104.9	7.2	187.7	4.4	9.9	29.4
151	1182				15.0	6.7	t.w. MPE	-6.69250	0.18	0.50257	0.18	-114.3	2.3	-203.9	2.3	152.5	97.7
152	37	E27	S2-9	I.16CC	11.2	2.1	Pau.	2.00265	0.13	0.55329	0.07	-75.6	1.4	244.4	1.1	246.2	29.8
153	52	E63	I.1W	I.1W	9.3	5.3	Pau.	5.26254	0.65	0.60162	0.72	-112.6	10.5	315.0	10.5	45.1	47.7
154	2	E39	I.16NE	I.16NE	9.2	3.1	Pau.	2.88734	0.24	0.99219	0.21	108.3	3.3	-356.7	2.8	-9.4	21.9
155	297				12.8	9.5	t.w.	9.44270	0.18	1.03930	0.26	52.2	3.2	-50.5	5.9	-251.9	37.4
156	16	E19	S1-9	R3 I.16NW	11.0	1.2	Gil.	0.08387	9.86	1.21967	10.09	236.2	0.3	26.8	0.3	-14.9	15.4
157	22	E31	S2-10	I.29N	11.0	2.1	Pau.	-1.58471	0.13	1.41130	0.13	186.0	0.7	-233.2	0.9	-189.5	94.8
158	691		S3-190	S3-190	14.1	3.5	Yel.	-3.16372	0.09	1.43188	0.13	-118.4	0.6	-127.1	0.7	-249.8	89.4

**Note.** Radial velocities determined in this work are annotated with this work—t.w., Trippe et al. (2008) is abbreviated Tri., Paumard et al. (2006) as Pau., Gillessen et al. (2017) as Gil., Yelda et al. (2014) as Yel. IRS stars are abbreviated as I.

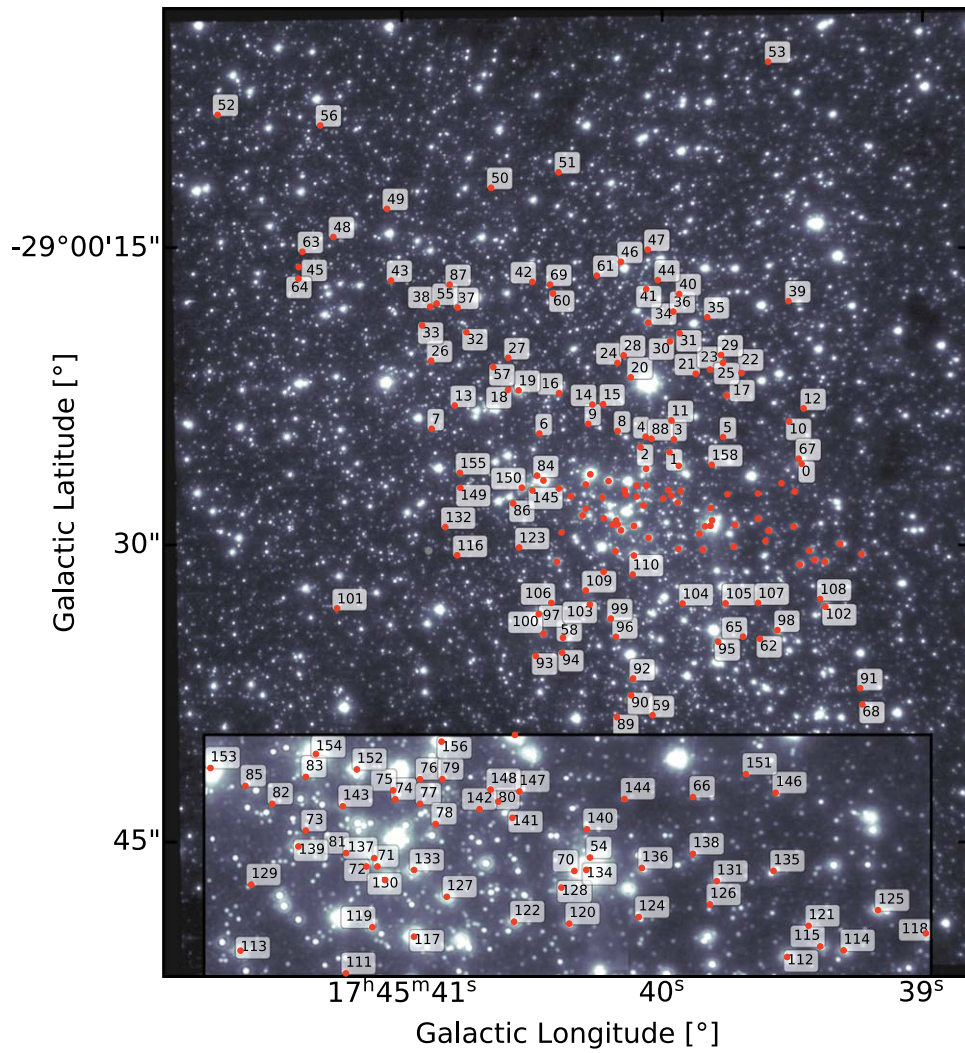


**Figure 22.** Lookup map of young stars without accelerations: young stars used in this study. The number indicated next to the star corresponds to the row index in column # in Table 5.



**Appendix K**

Tables 6, 7, 8, 9, and 10 give the name and properties of the respective members of features CW1, CW2, F1/CCW, F2, and F3.

**Table 6**  
Stars Consistent with Belonging to the Clockwise Disk

Delta Evidence	MPE	Mag	Orbit	Paumard	$R$	UCLA	index
1.23236	S31	15.85	yes	E7	0.140883	S0-8	8.0
0.284251	S67	12.35	yes	E15	0.785569	S1-3	15.0
0.257495	S66	14.80	yes	E17	0.91267	S1-2	17.0
0.111609	S96	10.75	yes	E20	1.01648	S1-11	18.0
0.151909	S91	12.72	yes		1.24012		19.0
0.156153	S83	13.73	yes	E16	0.970887	S0-15	20.0
0.122042	R14	13.2434	yes	E22	1.49567	S1-14	21.0
0.229224	S97	10.83	yes	E23	1.20495	S1-16	22.0
0.431062	R44	13.56	yes		2.39507	S2-21	23.0
0.150007	S87	14.23	yes	E21	1.88273	S1-12	24.0
0.0788419	R85	11.95	yes	E56	3.14758	IRS 34W	29.0
0.130773	R1	14.05	yes	E29	0.802778	S2-7	31.0
0.569367	S5	15.37	yes	E8	0.0669288	S0-26	32.0
0.127589	R39	12.21	yes	E40	1.77438	S3-5	34.0
0.359158	R30	11.58	yes	E32	2.42514	S2-15	35.0
1.21663		12.26	no	E35	2.29462	S2-16	NaN
1.30642		12.70	no	E36	2.34171	S2-19	NaN
1.21927		13.18	no	E38	2.77465	S2-74	NaN
1.29563		13.22	no	E61	4.70471		NaN
1.14487		13.81	no	E44	3.29133	S3-25	NaN
1.42171		14.78	no		6.96803		NaN
1.02538		12.31	no	E28	2.08402	S2-4	NaN
1.77592	S11	14.7349	no		0.647205	S0-9	NaN
1.34486		13.25	no	E76	9.11443	S9-20	NaN
1.08638		12.0764	no		8.28775	S8-7	NaN
1.99746		12.1135	no		8.81132		NaN
1.15591		10.96	no	E41	3.19491		NaN
1.32925		12.0253	no	E43	3.20321	S3-19	NaN
1.98846		12.73	no	E45	3.33866	S3-26	NaN
1.17552		11.24	no	E34	2.27189	S2-17	NaN
0.816577		14.47	no		10.3372	S10-32	NaN
1.02802		12.27	no	E30	2.09801	S2-6	NaN
0.752306		12.34	no	E50	3.53519	S3-10	NaN
1.13523		12.86	no	E25	1.69564	S1-22	NaN
1.72061		15.70	no		1.05415		NaN
1.25565		11.16	no	E27	2.07763	S2-9	NaN
1.07359		14.06	no		3.47266	S3-190	NaN

**Table 7**  
Stars Consistent with Belonging to the Counterclockwise Disk

Index	MPE	UCLA	Paumard	Mag	$R$	Delta Evidence	Orbit
7	S12	S0-19	E5	15.48	0.0306114	0.869801	yes
0		S7-216		10.8521	7.86087	1.48128	no
3		S3-17		13.49	3.17676	1.42991	no
6		S6-89		11.95	6.22556	1.91016	no
9			E59	13.14	4.55295	1.25763	no
11		S3-331	E52	13.60	3.84197	1.38002	no
13		S10-7	E85	12.59	10.6752	0.850875	no
15		S4-364	E62	12.14	4.99596	1.4844	no
16		S6-93	E70	12.74	6.66203	1.9463	no
18				12.14	8.67924	0.476479	no
25		S7-19		13.2978	7.5208	1.23329	no
26			E90	11.57	12.7703	1.14776	no
29		S7-20		13.3627	7.86642	1.18854	no
32				13.3406	12.2262	0.992025	no
35		S9-13		13.18	9.3076	1.67622	no
47			E89	14.44	12.2754	1.38127	no
52		outer-1		11.96	28.7782	1.28205	no
53		outer-2		14.867	22.4266	1.28966	no
56				15.8499	24.8177	1.35955	no
60				15.94	11.1737	1.57827	no
64				15.7765	20.6513	1.89283	no
67		S7-228		12.0222	7.92802	1.50092	no
75	S93			15.38	1.09141	1.80819	no
76	S26	S0-31	E13	15.4293	0.721656	1.65122	no
77	S7	S0-11	E12	15.5999	0.497586	1.6382	no
87				16.7216	14.4812	1.86302	no
90				13.7248	10.1881	1.44307	no
91				13.8585	14.4931	1.75828	no
100				12.2566	8.03726	1.12067	no
102				11.2038	10.6092	1.84185	no
118				13.1939	11.152	0.922799	no
123		S7-30		14.05	7.01209	1.2573	no
126				14.9965	6.36436	0.720289	no
136		S4-258	E60	12.45	4.67586	0.651513	no
149		S9-1	E78	12.76	9.46204	1.60932	no
155				12.7962	9.49969	1.37407	no

**Table 8**  
Stars Consistent with Belonging to the Inner Warp Feature

Index	MPE	UCLA	Paumard	Mag	$R$	Delta Evidence	Orbit
6	S60			16.76	0.113085	0.629584	yes
30	R70	S4-36	E54	12.82	2.08898	0.656347	yes
10		S7-236		12.666	7.94508	1.3941	no
30		S7-10	E73	11.62	7.70832	1.05606	no
36		S9-23	E77	13.57	9.23117	1.30484	no
40		S10-5	E83	11.97	10.1532	1.78867	no
65				15.3536	8.67658	1.53632	no
84		S5-237		13.25	5.59141	1.15228	no
85		S4-169	E57	13.53	4.43282	1.95868	no
86		S6-82	E72	13.56	6.73303	1.50384	no
96		S7-16		12.6886	7.42579	1.71009	no
99		S6-63	E69	11.36	6.57862	0.921401	no
103			E65	12.13	6.3003	1.06481	no
105				12.9989	6.79444	1.0242	no
106				12.2293	7.36999	1.69583	no
143		S2-22		13.03	2.33073	1.99339	no
145		S5-231	E64	12.01	5.81382	1.60709	no
150		S6-81	E67	11.08	6.3722	1.47119	no
153			E63	9.328	5.297	0.938662	no

**Table 9**  
Stars Consistent with Belonging on the Outer Warp of the Clockwise Disk

MPE	UCLA	Paumard	Mag	$R$	$\Delta$ Evidence	Orbit
S9	S0-5	E9	15.15	0.091365	1.38003	yes
S60	S5-235		16.76	0.113116	0.589293	yes
			13.21	5.33721	1.95023	no
			14.78	6.96797	0.958125	no
			13.71	7.06065	1.15084	no
			11.12	8.54245	0.321072	no
	S8-4	E75	11.12	8.54245	0.321072	no
	S9-23	E77	13.57	9.2312	0.983455	no
	S10-5	E83	11.97	10.1532	0.673866	no
	S10-4	E84	11.29	10.2412	0.360631	no
			13.8392	12.0786	1.61299	no
	S10-48	E86	15.11	10.7369	1.76352	no
	S11-5	E88	11.70	11.7584	1.19523	no
			13.87	19.3905	1.95884	no
	S11-21	E87	14.4037	16.7276	0.872181	no
			15.3588	11.2452	1.91458	no
			13.51	11.2396	0.531913	no
			15.3722	9.27017	1.86716	no
			15.3536	8.67654	1.52626	no
	S1-33		14.3489	15.152	1.82959	no
			15.06	1.2391	1.43069	no
	S2-58		14.04	2.45128	0.99258	no
	S4-169	E57	13.53	4.4328	1.72397	no
			16.7216	14.4813	1.87428	no
	S2-76		15.15	2.81263	1.45724	no
			12.6724	11.3924	1.95734	no
	S9-20	E76	11.4295	9.36258	0.50663	no
			13.25	9.11447	1.2888	no
	S7-16		12.6886	7.42576	0.981402	no
			12.1135	8.81131	1.71294	no
	S5-187		13.21	5.78784	1.15952	no
			12.2293	7.36998	1.94377	no
	S4-71	E55	12.61	4.13535	1.1851	no
	S3-30	E47	12.65	3.4013	1.13645	no
S3-374	E53	12.73	3.93736	1.02151	no	
S2-13	E33	11.71	2.19857	1.75181	no	
S1-24	E26	11.82	1.7597	1.69777	no	
S2-22		13.03	2.33074	1.45088	no	
S5-231	E64	12.01	5.81383	1.35316	no	
S7-161		13.6985	7.36771	1.74088	no	
		15.70	1.05406	1.95867	no	
S3-190		14.06	3.47265	1.7133	no	

**Table 10**  
Stars Consistent with Belonging on the Newly Detected Disk

MPE	UCLA	Paumard	Mag	$R$	$\Delta$ Evidence	Orbit
S4	S0-3	E6	14.58	0.091998	1.90794	yes
S14		E2	15.63	0.00271191	0.0173749	yes
S2		E1	14.16	0.0107373	1.44597	yes
			12.4966	11.3631	1.85805	no
	IRS10W		10.9925	8.29025	1.99354	no
		E90	11.57	12.7704	0.561536	no
			13.6698	9.79173	0.463197	no
			13.71	7.06064	1.24503	no
	S7-10	E73	11.62	7.70833	1.77437	no
	S8-15		13.20	8.19548	1.24777	no
			13.3406	12.2262	0.875552	no
			14.1015	13.2585	1.55044	no
			13.7893	14.4404	1.44733	no
			13.8392	12.0786	1.7897	no
			14.7092	20.9025	1.34779	no
			12.7599	20.3779	1.0109	no
			13.87	19.3904	0.882945	no
			14.4037	16.7275	1.21626	no
	outer-1		11.96	28.7817	1.22527	no
			15.4278	14.3609	0.223891	no
			15.0569	10.0754	0.611814	no
			15.94	11.1737	1.2928	no
	S11-21	E87	13.51	11.2396	1.53688	no
			15.3722	9.27012	0.551794	no
			16.6731	21.158	0.798925	no
			15.7765	20.651	1.18804	no
			15.41	5.64006	1.65611	no
			14.3489	15.152	0.281202	no
			16.5563	11.611	1.77148	no
		E46	10.703	3.38768	0.919629	no
	S2-4	E28	12.31	2.08402	1.69374	no
	S2-50		15.34	2.27306	0.983683	no
	S3-3		15.1047	3.14943	1.12699	no
S93			15.38	1.09142	1.20983	no
S7	S0-11	E12	15.5999	0.496342	1.10106	no
	S3-314		15.50	3.83191	1.05654	no
	S3-2		12.25	3.11262	1.6286	no
			16.7216	14.4813	0.294344	no
	S2-76		15.15	2.81263	1.73484	no
	S9-114	E79	11.00	9.48721	0.556273	no
			11.2038	10.6092	0.709141	no
	S5-187		13.21	5.78785	1.98491	no
	S4-196		14.4433	4.52485	1.68582	no
	S8-181	E74	11.88	8.41553	1.14199	no
			12.3832	9.51841	1.17089	no
	S9-143		12.8182	9.01071	1.68612	no
	S8-196		12.557	8.59268	1.07554	no
	S5-34		13.7426	5.09913	0.966934	no
	S3-26	E45	12.73	3.33865	1.81866	no
	S7-180	E58	13.5213	7.52872	1.9775	no
	S2-6	E30	12.27	2.098	1.8105	no
	S5-236		13.2592	5.70296	1.91062	no
	S7-161		13.6985	7.3677	1.75061	no


### ORCID iDs


Sebastiano D. von Fellenberg  <https://orcid.org/0000-0002-9156-2249>

Stefan Gillessen  <https://orcid.org/0000-0002-5708-0481>

Reinhard Genzel  <https://orcid.org/0000-0002-2767-9653>

Tim de Zeeuw  <https://orcid.org/0000-0003-4175-3474>

Antonia Drescher  <https://orcid.org/0000-0002-4494-5503>

Maryam Habibi  <https://orcid.org/0000-0003-1366-1695>

Thomas Ott  <https://orcid.org/0000-0003-1572-0396>

Felix Widmann  <https://orcid.org/0000-0002-0327-6585>

### References

- Ali, B., Paul, D., Eckart, A., et al. 2020, *ApJ*, 896, 100  
Bahcall, J. N., & Wolf, R. A. 1976, *ApJ*, 209, 214  
Bartko, H., Martins, F., Fritz, T. K., et al. 2009, *ApJ*, 697, 1741  
Bartko, H., Martins, F., Trippe, S., et al. 2010, *ApJ*, 708, 834

- Becklin, E. E., & Neugebauer, G. 1968, *ApJ*, 151, 145
- Becklin, E. E., & Neugebauer, G. 1975, *ApJL*, 200, L71
- Beloborodov, A. M., Levin, Y., Eisenhauer, F., et al. 2006, *ApJ*, 648, 405
- Blum, R. D., Sellgren, K., & Depoy, D. L. 1996, *ApJ*, 470, 864
- Boehle, A., Ghez, A. M., Schödel, R., et al. 2016, *ApJ*, 830, 17
- Bonnell, I. A., & Rice, W. K. M. 2008, *Sci*, 321, 1060
- Bonnet, H., Conzelmann, R., Delabre, B., et al. 2004, *Proc. SPIE*, 5490, 130
- Chen, X., & Amaro-Seoane, P. 2014, *ApJL*, 786, L14
- Do, T., Lu, J. R., Ghez, A. M., et al. 2013, *ApJ*, 764, 154
- Fritz, T. K., Gillessen, S., Dodds-Eden, K., et al. 2011, *ApJ*, 737, 73
- Gallego-Cano, E., Schödel, R., Dong, H., et al. 2018, *A&A*, 609, A26
- Genzel, R., Hollenbach, D., & Townes, C. H. 1994, *RPPH*, 57, 417
- Genzel, R., Pichon, C., Eckart, A., Gerhard, O. E., & Ott, T. 2000, *MNRAS*, 317, 348
- Genzel, R., Schödel, R., Ott, T., et al. 2003, *ApJ*, 594, 812
- Ghez, A. M., Morris, M., Becklin, E. E., Tanner, A., & Kremenek, T. 2000, *Natur*, 407, 349
- Gillessen, S., Eisenhauer, F., Trippe, S., et al. 2009, *ApJ*, 692, 1075
- Gillessen, S., Plewa, P. M., Eisenhauer, F., et al. 2017, *ApJ*, 837, 30
- Giral Martínez, J., Fouvry, J.-B., & Pichon, C. 2020, *MNRAS*, 499, 2714
- Gravity Collaboration, Abuter, R., Amorim, A., et al. 2021, *A&A*, 647, A59
- Gravity Collaboration, Abuter, R., Aymar, N., et al. 2022, *A&A*, 657, L12
- Habibi, M., Gillessen, S., Martins, F., et al. 2017, *ApJ*, 847, 120
- H.E.S.S. Collaboration, Abdalla, H., Abramowski, A., et al. 2018, *A&A*, 612, A1
- Hobbs, A., & Nayakshin, S. 2009, *MNRAS*, 394, 191
- Kocsis, B., & Tremaine, S. 2011, *MNRAS*, 412, 187
- Kocsis, B., & Tremaine, S. 2015, *MNRAS*, 448, 3265
- Krabbe, A., Genzel, R., Drapatz, S., & Rotaciuc, V. 1991, *ApJL*, 382, L19
- Kroupa, P. 2001, *MNRAS*, 322, 231
- Levin, Y., & Beloborodov, A. M. 2003, *ApJL*, 590, L33
- Li, T. P., & Ma, Y. Q. 1983, *ApJ*, 272, 317
- Löckmann, U., & Baumgardt, H. 2009, *MNRAS*, 394, 1841
- Lu, J. R., Do, T., Ghez, A. M., et al. 2013, *ApJ*, 764, 155
- Lu, J. R., Ghez, A. M., Hornstein, S. D., et al. 2006, in *Journal of Physics: Conf. Series, Proc. of The Universe Under the Microscope - Astrophysics at High Angular Resolution, Galactic Center Youth: Orbits and Origins of the Young Stars in the Central Parsec*, 54, ed. R. Schoedel et al. (Bristol: IOP Publishing), 279
- Lu, J. R., Ghez, A. M., Hornstein, S. D., et al. 2009, *ApJ*, 690, 1463
- Madigan, A.-M., Pfuhl, O., Levin, Y., et al. 2014, *ApJ*, 784, 23
- Nayakshin, S. 2006, *MNRAS*, 372, 143
- Nayakshin, S., Cuadra, J., & Springel, V. 2007, *MNRAS*, 379, 21
- Paumard, T., Genzel, R., Martins, F., et al. 2006, *ApJ*, 643, 1011
- Perets, H. B., & Gualandris, A. 2010, *ApJ*, 719, 220
- Perets, H. B., Gualandris, A., Kuzi, G., Merritt, D., & Alexander, T. 2009, *ApJ*, 702, 884
- Pfuhl, O., Alexander, T., Gillessen, S., et al. 2014, *ApJ*, 782, 101
- Pfuhl, O., Fritz, T. K., Zilka, M., et al. 2011, *ApJ*, 741, 108
- Salpeter, E. E. 1955, *ApJ*, 121, 161
- Schödel, R., Gallego-Cano, E., Dong, H., et al. 2018, *A&A*, 609, A27
- Schödel, R., Noguera-Lara, F., Gallego-Cano, E., et al. 2020, *A&A*, 641, A102
- Schödel, R., Ott, T., Genzel, R., et al. 2003, *ApJ*, 596, 1015
- Simons, D. A., & Becklin, E. E. 1996, *AJ*, 111, 1908
- Skilling, J. 2004, in *AIP Conf. Ser. 735, Bayesian Inference and Maximum Entropy Methods in Science and Engineering: 24th Int. Workshop on Bayesian Inference and Maximum Entropy Methods in Science and Engineering*, ed. R. Fischer, R. Preuss, & U. V. Toussaint (Melville, NY: AIP), 395
- Skilling, J. 2006, *BayAn*, 1, 833
- Speagle, J. S. 2020, *MNRAS*, 493, 3132
- Stewart, I. M. 2009, *A&A*, 495, 989
- Støstad, M., Do, T., Murray, N., et al. 2015, *ApJ*, 808, 106
- Szölgvény, Á., & Kocsis, B. 2018, *PhRvL*, 121, 101101
- Trippe, S., Gillessen, S., Gerhard, O. E., et al. 2008, *A&A*, 492, 419
- Yelda, S., Ghez, A. M., Lu, J. R., et al. 2014, *ApJ*, 783, 131